LAND SURFACE TEMPERATURE

VISIBLE/INFRARED IMAGER/RADIOMETER SUITE ALGORITHM THEORETICAL BASIS DOCUMENT

Version 4: May 2001

Donglian Sun
Yimin Ji
Philip E. Ardanuy
Peter S. Kealy
Wenli Yang

William Emery, Science Team Member
University of Colorado

RAYTHEON SYSTEMS COMPANY
Information Technology and Scientific Services
4400 Forbes Boulevard
Lanham, MD 20706

SBRS Document #: Y2399

EDR: LAND SURFACE TEMPERATURE

Doc No: Y2399

Version: 4

Revision: 0

	Function	Name	Signature	Date
Prepared by	EDR Developer	D. SUN		
Edited by	Editor	P. KEALY		
Approved by	Chief Scientist	S. MILLER		
Released by	Algorithm IPT Lead	P. KEALY		

TABLE OF CONTENTS

Page

LIST OF FIGURES

LIST OF TABLES

GLOSSARY OF ACRONYMS

ATBD	Algorithm Theoretical Basis Document
ATSR	Along Track Scanning Radiometer
AVHRR	Advanced Very High Resolution Radiometer
ECMWF	European Center for Medium-Range Weather Forecast
EDR	Environmental Data Record
FOV	Field of View
IFOV	Instantaneous Field of View
IPO	Integrated Program Office
IR	Infrared
LST	Land Surface Temperature
MODIS	Moderate Resolution Imaging Spectroradiometer
MODTRAN	Moderate Resolution Atmospheric Radiance and Transmittance Model
MOSART	Moderate Spectral Atmosphere Radiance and Transmittance
NCEP	National Centers for Environment Prediction
NDVI	Normalized Difference Vegetation Index
NEDT	Noise Equivalent Temperature Difference
NPOESS	National Polar-orbiting Operational Environmental Satellite System
RSS	Root Sum Square
SBRS	Santa Barbara Remote Sensing
SST	Sea Surface Temperature
SWIR	Shortwave Infrared
TAR	Top of Atmosphere Radiance
TIR	Thermal Infrared
TOA	Top of Atmosphere
TPW	Total Precipitable Water
VIIRS	Visible/Infrared Imager/Radiometer Suite

ABSTRACT

This is the Algorithm Theoretical Basis Document (ATBD) for the National Polar-orbiting Operational Environmental Satellite System (NPOESS) Visible/Infrared Imager/ Radiometer Suite (VIIRS) Land Surface Temperature (LST) algorithm. LST is a VIIRS level 2 product and also an input variable for other VIIRS products such as soil moisture, land type classification, and infrared (IR)-band emissivity.

The atmospheric correction, the complexity of land surface types, and the sensor performance limit the accuracy of satellite LST measurements. The current satellite multi-channel LST algorithm can permit global LST retrievals on spatial scales of 8 km with 3 to 4 K measurement accuracy. The VIIRS LST Environmental Data Record (EDR) has a spatial resolution of 1.3km at the Edge-Of-Swath with 2.5 K measurement accuracy and 0.5 K measurement precision.

The VIIRS LST algorithms are based on physical regression methods to retrieve skin LST. They will use radiances sensed by VIIRS visible and IR channels. Two algorithms are being developed using a global database and a radiative transfer model.

The baseline algorithm establishes one equation for each land cover type and uses 4 thermal band brightness temperatures. This algorithm does not need emissivity information and yields better precision.

In the backup algorithm, radiances from visible and near-IR channels will be used to determine land cover type and the Normalized Difference Vegetation Index (NDVI). Emissivities for all IR bands for a certain land cover type will be calculated according to the land cover type classification and NDVI value. This will be done by use of a kernel model or a spectral library. The LST will be determined by emissivities and brightness temperatures derived from VIIRS IR 10.8, 12, and 8.55 µm bands.

Pre-launch and post-launch activities are discussed in this document. The validation of LST is limited by the availability of *in situ* observations. The VIIRS LST is defined as the skin temperatures of the uppermost layer of the land surface, while *in situ* observations are usually shelter temperatures. Reliable observed or analyzed skin temperatures will be a critical factor in validating the VIIRS LST retrieval.

1.0 INTRODUCTION

1.1 PURPOSE

This is the Algorithm Theoretical Basis Document (ATBD) for the National Polar-orbiting Operational Environmental Satellite System (NPOESS) Visible/Infrared Imager/ Radiometer Suite (VIIRS) Land Surface Temperature (LST) algorithm. This document identifies sources of input data, and describes the theoretical basis and development process of the LST algorithms.

1.2 SCOPE

LST is a VIIRS level 2 product and also an input variable for other VIIRS products, such as soil moisture. The LST algorithms described in this document will be used to routinely retrieve LSTs from VIIRS measurements. However, future development efforts may result in modifications to the current operational algorithms.

The next section of this document provides an overview of the LST retrieval algorithm. A description of the algorithms and their development is presented in Section 3. Section 3 also addresses error budgets, algorithm sensitivity, and validation. Constraints, assumptions, and limitations are identified in Section 4, and Section 5 presents references cited in the document.

1.3 VIIRS DOCUMENTS

Reference to VIIRS documents will be indicated by a number in italicized brackets, e.g., *[V-1]*.

[V-1] VIIRS Sensor Requirements Document, NPOESS IPO
[V-2] VIIRS Sea Surface Temperature ATBD, SBRS Doc. Y 2386

1.4 REVISIONS

This is the fourth version of this document, dated May 2001. The first version was dated October 1998. The second version was dated June 1999 and the third May 2000. This version has been significantly edited to improve readability and logical flow. Flowdown information has been removed. Version 5 will contain a detailed description of data flows and flag requirements.

2.0 EXPERIMENT OVERVIEW

2.1 OBJECTIVES OF LAND SURFACE TEMPERATURE RETRIEVALS

Land surface temperatures play an important role in land-surface processes on a regional as well as on a global scale. They are of fundamental importance to the net radiation budget at the Earth's surface and to monitoring the state of crops. LST is a good indicator of both the greenhouse effect and the energy flux between the atmosphere and the ground (Mannstein, 1987; Sellers *et al*., 1988). Satellite-derived LST can be assimilated to climate, mesoscale and land surface models to estimate the sensible heat flux and latent heat flux from the Earth's surface. Satellite-based LST measurement has not been used operationally in regional weather forecasting and climate prediction due to large uncertainties. However they have the potential to provide LST information over vast remote regions such as deserts.

The accuracy of satellite LST measurement is primarily limited by the atmospheric correction, the complexity of land surface types, and sensor performance. The current satellite multichannel LST algorithm can permit global LST retrievals on spatial scales of 8 km with 3 to 4 K measurement accuracy. (Becker and Li, 1990; Dozier and Wan, 1994; Li and Becker, 1993).

The overall scientific objective of the VIIRS LST retrievals is to provide improved measurements of global and regional LST fields. The VIIRS LST Environmental Data Record (EDR) requires a global horizontal cell size of 1.3 km with 2.5 K measurement accuracy and 0.5 K measurement precision. These requirements exceed the current state-of-the-art results. The requirement of measurement precision is difficult to meet because of the large variations of LST in both space and time. LSTs can vary by 10 K in just a few meters and by 50 K over the daily cycle (Prata, 1993).

2.2 INSTRUMENT CHARACTERISTICS

The VIIRS sensor is being designed based on the NPOESS sensor requirements derived from EDR system specifications. VIIRS bands in the far-infrared (IR) region have been placed to optimize their use for SST determination. Bands in the far-IR are usually located near the maximum Earth radiance. The influence of ozone and other atmospheric absorbers should be avoided. Figure 1 shows Moderate Resolution Atmospheric Radiance and Transmittance Model (MODTRAN) simulated radiances at satellite altitude for thermal infrared spectra. There are a total of five standard atmospheres shown. There are two wavelength regions suitable for far-IR band selection: 8–9 µm and 10–13 µm. VIIRS far-IR bands will be located in the two spectral regions. Figure 2 shows the MODTRAN simulated atmospheric transmittance for five standard atmospheres. It shows that the 8–9 µm and 10–13 µm regions are transparent to the atmosphere. The details of LST band selection can be found in Caselles *et al*., 1997, however VIIRS bands were optimized for SST.

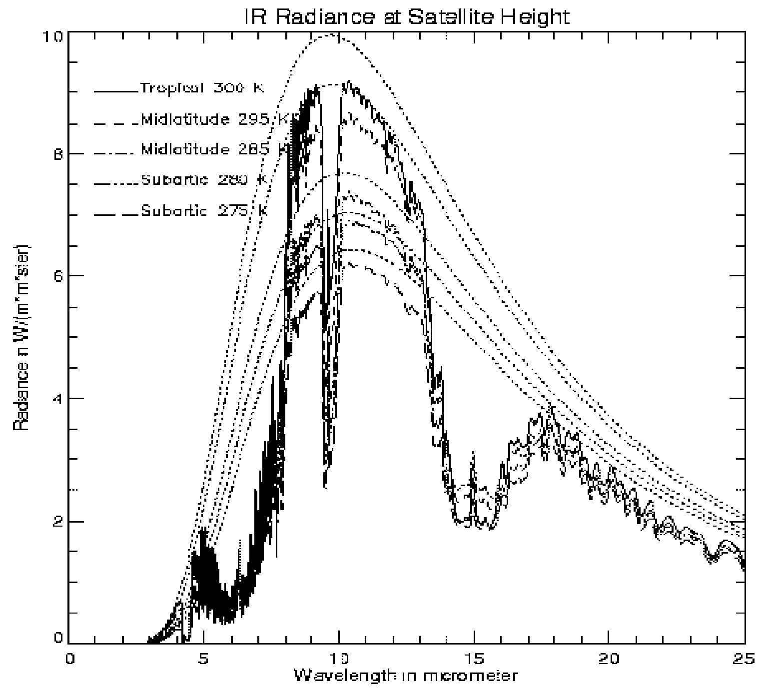

Figure 1. IR radiance at the satellite for five atmospheres simulated by MODTRAN. The dashed lines are calculated from the Planck function.

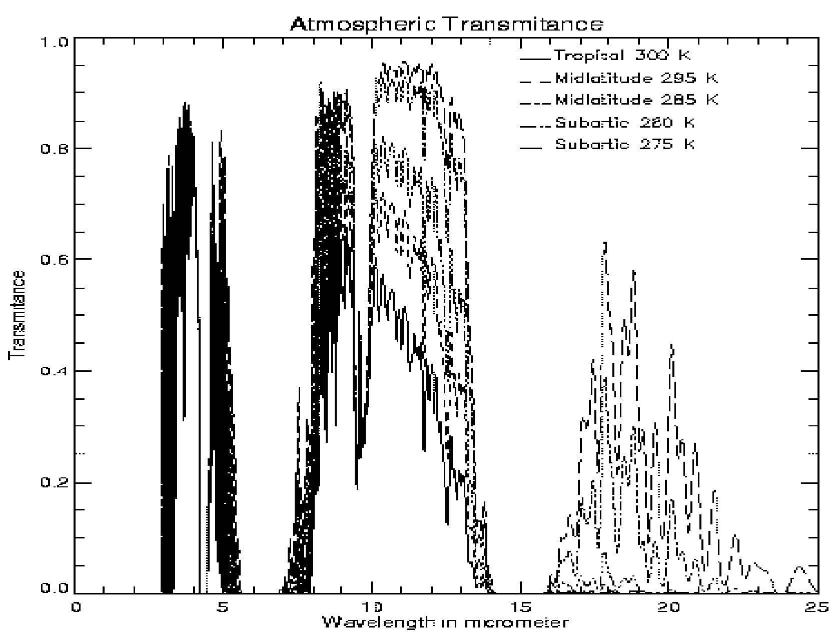

Figure 2. Atmospheric transmittances for five atmospheres. The dashed lines are calculated from the Planck function.

2.3 LAND SURFACE TEMPERATURE RETRIEVAL STRATEGIES

To solve the Land Surface Temperature problem physically is not easy. We must know the atmospheric profile for each pixel (unlikely to be available in the near future), and also the surface emissivity for each band. Because the surface emissivity for each band is different, the number of unknowns is always larger than the number of equations discussed above. A number of ways have been suggested to physically retrieve the surface temperature and emissivity. These methods include the two temperature method (Watson, 1992), the temperature emissivity separation method (Kealy and Hook, 1993), and the day/night method (Wan and Dozier, 1996). However, these methods demand many more far-IR bands than in the VIIRS baseline design. During the earlier phases of development many LST approaches were considered and are summarized below. Of these many approaches two have been selected. The baseline and backup algorithms are described in section 3.

(1) Regression methods (Emissivity approach)

1A. Generalized Split Window:

Split Window (10.8, 12 μm bands) Algorithm (Wan and Dozier (1996), based on Becker and Li's 1990 algorithm):

$$T_s = a_0 + (a_1 + a_2\varepsilon_1 + a_3\varepsilon_2)T_1 + (a_4 + a_5\varepsilon_1 + a_6\varepsilon_2)T_2$$

Where $\varepsilon_1 = \dfrac{1-(\varepsilon_{11}+\varepsilon_{12})/2}{(\varepsilon_{11}+\varepsilon_{12})/2}$, $\varepsilon_2 = \dfrac{\varepsilon_{11}-\varepsilon_{12}}{((\varepsilon_{11}+\varepsilon_{12})/2)^2}$, and ε_{11} and ε_{12} are emissivities corresponding to 10.8 and 12.0 μm bands, respectively.

$T_1 = (T_{11}+T_{12})/2$ and $T_2 = T_{11}-T_{12}$ where T_{11} and T_{12} are brightness temperature at 10.8 and 12.0 μm bands, respectively.

1B. Three band Algorithm (Backup Solution):

A 3-band algorithm (10.8, 12, 8.55 μm bands)

$$T_S = a_0 + a_1\frac{(1-\varepsilon_{10.8})}{\varepsilon_{10.8}}T_{10.8} + a_2\frac{(1-\varepsilon_{12})}{\varepsilon_{12}}T_{12} + a_3\frac{(1-\varepsilon_{8.55})}{\varepsilon_{8.55}}T_{8.55} + a_4(\sec\theta - 1)$$

1C. Five band (10.8, 12, 8.55, 3.75, 4.005 μm bands) Algorithm:

$$T_S = a_0 + a_1\frac{(1-\varepsilon_{10.8})}{\varepsilon_{10.8}}T_{10.8} + a_2\frac{(1-\varepsilon_{12})}{\varepsilon_{12}}T_{12} + a_3\frac{(1-\varepsilon_{8.55})}{\varepsilon_{8.55}}T_{8.55} + a_4(\sec\theta - 1)) + a_5T_{3.75} \quad + a_6\ T_{3.75}$$

(2) Land Cover approach Regression methods

2A. Two band Algorithm:

For each of the VIIRS 21 surface types, establish one equation by using 11 and 12 micron split window.

$$LST_i = a_0(i) \quad + a_1(i)\, T_{11} + a_2(i)\, (T_{11} - T_{12}) + a_3(i)\, (\sec\theta - 1) + a_4(i)\, (T_{11} - T_{12})^2 \qquad i = 1,\ 21$$

2B. Four band Algorithm (Baseline Solution):

VIIRS-4 band day/night LST algorithm establishes one equation for each surface type by using 4 VIIRS bands (10.8, 12, 3.75, and 4.005 μm), with added solar zenith angle correction during the daytime:

Daytime:

$$\begin{aligned} LST_i = {} & a_0(i) + a_1(i)T_{11} + a_2(T_{11} - T_{12}) + a_3(i)(\sec\theta - 1) + a_4(i)T_{3.75} + a_5(i)T_{4.0} + a_6(i)T_{3.75}\cos\varphi \\ & + a_7(i)T_{4.0}\cos\varphi + a_9(i)(T_{11} - T_{12})^2 \qquad i = 1,\ 21 \end{aligned}$$

Nighttime or day and night:

$$\begin{aligned} LST_i = {} & b_0(i) + b_1(i)T_{11} + b_2(T_{11} - T_{12}) + b_3(i)(\sec\theta - 1) + b_4(i)T_{3.75} + b_5(i)T_{4.0} + b_6(i){T_{3.75}}^2 \\ & + b_7(i){T_{4.0}}^2 + b_9(i)(T_{11} - T_{12})^2 \qquad i = 1,\ 21 \end{aligned}$$

Where i is the index of 21 VIIRS surface types.

Without the solar zenith angle correction, the equation above is used for both day and nighttime.

2C. Five band Algorithm:

A potential VIIRS-5 band LST algorithm can be used to establish one equation to each surface type by using 5 VIIRS bands (10.8, 12, 3.75, 4.005 and 8.55 μm).

(3) Physical Retrieval Approach

(a) Linearize the Radiative Transfer Equation (RTE)

Linearize the radiative transfer equation with the nonlinearized terms being handled by physical kernel functions or Jacobians. Solve the linearized radiative transfer equations with the nonlinearities being handled through an optimized numerical iteration procedure (Marquardt-Levenberg Iteration) to get the surface skin temperature, atmospheric profiles (Temperature, Water vapor, Ozone) and surface emissivities. In order to retrieve surface properties, we need to select some window channels. In our work, we select 7 channels which are atmospheric windows or more surface-sensitive, and we assume the channel indexes are:

k_1, k_2, ….., k_7.

For the single Field of View (FOV), the linearized RTE for the channel j is:

$$\delta TB = K_{T_s}\delta T_s + \int_0^{p_s} K_T \delta T dP + \int_0^{P_s} K_q \delta \ln q\, dp + K^*{}_{\varepsilon e_1}\delta\varepsilon_1 + K_{\varepsilon_2}{}^*\delta\varepsilon_2 + \cdots + K_{\varepsilon_7}{}^*\delta\varepsilon_7$$
$$+ K_{\rho_1}{}^*\ \delta\rho_1 + K^*\delta\rho + \cdots + K_{\rho_7}{}^*\delta\rho_7 + K_N\delta N + K_{p_c}\delta P_c \tag{1}$$

Where TB is the brightness temperature, T_s is the surface skin temperature, T is the temperature profile, q is the water vapor profile, ε_1, ε_2, … ε_7 are the surface emissivities for 7 window channels, ρ_1, ρ_2, … ρ_7 are the surface reflectance for the seven window channels. N is the cloud fraction, P_c is the cloud top pressure. K is the physical kernel function or Jacobians for the the corresponded term.

$$K_{\varepsilon_i} = \partial TB_{k_i} / \partial\varepsilon$$

$$K\rho_i{}^* = \xi(k_i, j)K_{\rho_i}$$

$$K_{\varepsilon_i} = \xi(k_i, j)\, K_{\varepsilon_i}$$

$$\xi(k,j) = \begin{cases} 1 & k = j \\ 0 & k \neq j \end{cases}$$

k_i=1, 2, … 7

Equation (1) can be written in a more compact form as,

$$\delta y = K\delta x \tag{2}$$

Where $\delta y = \delta TB$. The Jacobian K is a matrix containing the Jacobians in (1)

$$K = [\ K_{Ts}\ K_T\ K_q\ K_{\varepsilon 1}\ ...K_{\varepsilon 7}\ K_{\rho 1}...K_{\varepsilon 7}\ K_N\ K_{Pc}]$$

And δx is a vector of the variables to be retrieved,

$$\delta x = [\delta T_s\ \delta T\ \delta\varepsilon_1\ ...\delta\varepsilon_7\ \delta\rho_1\ ...\delta\rho_7\ \delta N\ \delta Pc\ ]^T$$

(b) Marquardt-Levenberg retrieval algorithm

This retrieval algorithm uses a hybrid nonlinear Newtonian iteration scheme, called the Marquardt-Levenberg method to find the maximum likelihood solution.

The Marquardt-Levenberg method is formulated as:

$$x_{n+1} = x_n - [\nabla^2 J(x_n) + \gamma I]^{-1} \nabla J(x_n)$$

Where γ is a parameter used to control the rate of convergence, J(x) is the probability density function defined as,

$$J(x) = (x - x_b)^T S_b^{-1} (x - x_b) + (y - F(x))^T (y - F(x))$$

Where x is the state vector, x_b is the initial state and S_b is its expected error covariance matrix. S is the expected covariance of the combined measurement and forward model error. Y is a vector of brightness temperature measurements, and F(x) is the forward model.

Therefore, the maximum likelihood solution by using Marquardt-Levenberg iteration is given as:

$$X_{n+1} = X_b + (K_n^T S^{-1} K_n + S_b^{-1} + \gamma I)^{-1} [K_n^T S^{-1} ((y - F(X)) + K_n (X_n - X_b)) + \gamma I (X_n - X_b)] \quad (3)$$

(c) Convergence Criteria

Each iteration of Equation 3 required the application of a convergence test to determine whether the solution is or is not convergent. The γI matrix may then be adjusted based on the result of the convergence test. The convergence test applied to the Marquardt-Levenberg iteration determines the fit between the measurements and solution in terms of the "distance" between two consecutive solution sets:

$$d_{n=1} = (x_{n+1} - x_n)^T \left(K_n^T S^{-1} K_n + \gamma I\right)^{-1} (x_{n+1} - x_n)$$

with d_{n+1} being the "distance" between solutions x_{n+1} and x_n. If $d_{n+1} < d_n$, meaning the solution is converging, the γI elements are decreased and the state vector solution is updated. However, for the divergent solution, $d_{n+1} \geq d_n$, the γI elements are increased and the iteration is repeated with the "same state vector x" that was used in the previous iteration.

(4) Physical retrieval combined with statistical retrieval

Starting from the radiative transfer equation, the radiance measured by the channel i of a satellite sensor can be written as:

$$B_i(T_i) = \tau_i [\varepsilon_i B_i(T_s) + \rho_i \, R_i^{\downarrow}] + R_i^{\uparrow} \quad (4)$$

Where B_i is Plank function weighted for channel i, T_i is the rightness temperature measured at satellite level in the channel i, τ_I is the atmospheric transmittance for channel i, $R_i^{\downarrow}$ is the hemispheric downward atmospheric radiance for the waveband of channel i, $R_i^{\uparrow}$ is the upward radiance emitted by the atmosphere in the waveband of channel i, ρ_i is the channel bi-directional reflectivity of the surface. For simplicity, we assume Lambertian reflection, this is $\rho_i=(1-\varepsilon_i)$.

Define brightness temperature at surface level T_i^*:

$$B_i(T_i^*) = \varepsilon_i B_i(T_s) + (1-\varepsilon_i) R_i^{\downarrow} \tag{5}$$

Define mean radiative temperature of the atmosphere in the upward direction $T_a^{\uparrow}$, and downward direction $T_a^{\downarrow}$:

$$B_i(T_a^{\uparrow}) = \frac{R_i^{\uparrow}}{1-\tau_i}, \qquad B_i(T_a^{\downarrow}) = \frac{R_i^{\downarrow}}{1-\tau_i}$$

Then inserting Equation 5 into Equation 4:

$$B_i(T_i) = \tau_i\, B_i(T_i^*) + (1-\tau_i)\, B_i(T^{\uparrow}{}_a)$$

Linearize the Plank function around T_i:

$$\frac{\partial B}{\partial T}\Big|_{T_i}\; L(T_i) = \tau_i \frac{\partial B}{\partial T}\Big|_{T_i}\; (T_i^* - T_i + L(T_i)) + (1-\tau_i)\frac{\partial B}{\partial T}\Big|_{T_i}\; (T_a^{\uparrow} - T_i + L(T_i))$$

$$L(T_i) = B_i(T_i) / \frac{\partial B}{\partial T}\Big|_{T_i}$$

The Planck function can be well approximated using a simple power function (Price, 1989):

$$B_i(T_i) = \alpha_i\, T^{n_i}$$

Parameters α_i and n_i are constants obtained by a least-square regression fitting. In order to have the best approximation of the Planck function, we divide the temperature range into two parts, less than 285 K, and warmer than 285 K. The parameter n_i is compiled in Table 1 in each case.

Table 1. Parameter n_i for Approximate Planck Function (Power Function) for Five VIIRS Bands

Channel (µm)	n_i (T_i<285 K)	n_i (T_i>285 K)
3.75	13.87795	12.89512
10.8	4.99027	4.57420
12	4.51020	4.15224
4.005	13.32985	12.19271
8.55	6.27005	5.76009

The power law approximation is very useful for analyses involving the Planck function, with this approximation.

$$L\,(T_i) = \frac{T_i}{n_i}$$

So the atmospheric correction for brightness temperature can be written as:

$$T_i^* = T_i + \frac{1-\tau_i}{\tau_i}(T_i - T_a^{\uparrow}) = \frac{1}{\tau_i}T_i - \frac{1-\tau_i}{\tau_i}T_a^{\uparrow} \tag{6}$$

T_i^* depends only on the spectral because of its spectral dependence of surface emissivity. We linearize Planck function around T_i^* obtaining the emissivity correction, this is:

$$Ts = T_i^* + \frac{(1-\varepsilon_i)}{\varepsilon_i}\left[\frac{T_i^*}{n_i} + \frac{(n_i-1)}{n_i}(1-\tau_i)T_i^* - (1-\tau_i)T_a^{\downarrow}\right] \tag{7}$$

Inserting Equation 6 into Equation 7, we get:

$$T_s = C_{1i}T_i - C_{2i}T_a^{\uparrow} - C_{3i}T_a^{\downarrow}$$

Where:

$$C_{1i} = \frac{1}{\tau_i}\left[1 + \frac{(1-\varepsilon_i)}{n_i\varepsilon_i} + \frac{(1-\varepsilon_i)(1-\tau_i)(n_i-1)}{n_i\varepsilon_i}\right]$$

$$C_{2i} = \frac{(1-\tau_i)}{\tau_i}\left[1 + \frac{(1-\varepsilon_i)}{n_i\varepsilon_i} + \frac{(1-\varepsilon_i)(1-\tau_i)(n_i-1)}{n_i\varepsilon_i}\right]$$

$$C_{3i} = \frac{(1-\varepsilon_i)}{\varepsilon_i}(1-\tau_i)$$

Suppose surface emissivity and the atmospheric transmittance are known, and n_i is a constant that depends on the spectral channel. So now we have the three unknown parameters T_s, $T_a^{\uparrow}$ and $T_a^{\downarrow}$, and we can only use the information of three channels to resolve the equation to obtain the surface temperature. In order to take advantage of all the information we can get, we can choose to use 3 bands to solve the equations, assume the channel indexes are: k1, k2, k3

$$Ts = C_{1k_1}T_{k_1} - C_{2k_1}T_a^{\uparrow} - C_{3k_1}T_a^{\downarrow}$$
$$Ts = C_{1k_2}T_{k_2} - C_{2k_2}T_a^{\uparrow} - C_{3k_2}T_a^{\downarrow}$$
$$Ts = C_{1k_3}T_{k_3} - C_{2k_3}T_a^{\uparrow} - C_{3k_3}T_a^{\downarrow}$$

$$T_a^{\uparrow} = \frac{(C_{3k_3} - C_{3k_2})(C_{1k_3}T_{k_3} - C_{1k_2}T_{k_2}) - (C_{3k_2} - C_{3k_1})(C_{1k_2}T_{k_2} - C_{1k_1}T_{k_1})}{(C_{2k_3} - C_{2k_2})(C_{3k_3} - C_{3k_2}) - (C_{3k_2} - C_{3k_1})(C_{2k_2} - C_{2k_1})}$$

$$T_a^{\downarrow} = \frac{(C_{1k_1}T_{k_1} - C_{1k_2}T_{k_2})}{(C_{3k_1} - C_{3k_2})} - \frac{(C_{2k_1} - C_{2k_2})}{(C_{3k_1} - C_{3k_2})}T_a^{\uparrow}$$

$$Ts = C_{1k_1}T_7 - C_{2k_1}T_a^{\uparrow} - C_{3k_1}T_a^{\downarrow}$$

If we know the surface emissivity and the atmospheric transmittance for three channels, we can calculate the surface temperature Ts according to Equation 3, so this algorithm is actually a physical retrieval approach. In our IPO data set, we did simulations of all 2415 profiles under clear conditions over land surface. We have calculated the atmospheric transmittance for each profile and can use this new physical algorithm.

In MODTRAN's standard atmosphere profiles, we can also calculate their atmospheric transmittance, as shown in Table 2.

Table 2. Atmospheric Transmittance for Standard Atmosphere Profiles

Atmosphere	Precipitable water(g/cm-2)	$\tau_{10.8}$	τ_{12}
U.S. standard	1.13	0.8552	0.8014
Tropical	3.32	0.5574	0.4159
Midlatitude summer	2.36	0.6915	0.5786
Midlatitude winter	0.69	0.8993	0.8646
Subarctic summer	1.65	0.7847	0.7011
Subarctic winter	0.33	0.9336	0.9147

In the event that the atmospheric transmittance not available, we can use these typical atmosphere's transmittance, and then combined with the regression method to find the appropriate coefficients for each term in the above Equation:

$$C_{ji} = a_0(j) + a_1(j)\frac{(1-\varepsilon_i)}{\varepsilon_i}, \quad j = k_1, k_3$$

Ts can then be written as:

$$Ts = a_0 + a_1 T_{k_1} + a_2 T_{k_2} + a_3 T_{k_3} + a_4 \frac{(1-\varepsilon_{k_1})}{\varepsilon_{k_1}} T_{k_1} + a_5 \frac{(1-\varepsilon_{k_2})}{\varepsilon_{k_2}} T_{k_2} + a_6 \frac{(1-\varepsilon_{k_3})}{\varepsilon_{k3}} T_{k_3}$$

If we add limb dark (view zenith angle) correction, then:

$$Ts = a_0 + a_1 T_{k_1} + a_2 T_{k_2} + a_3 T_{k_3} + a_4 \frac{(1-\varepsilon_{k_1})}{\varepsilon_{k_1}} T_{k_1} + a_5 \frac{(1-\varepsilon_{k_2})}{\varepsilon_{k_2}} T_{k_2}$$

$$+ a_6 \frac{(1-\varepsilon_{k_3})}{\varepsilon_{k3}} T_{k_3} + a_7(\sec\theta - 1)$$

(5) Further LST algorithms

There are many published LST algorithms available that were tested and are summarized briefly below. In recent years, some scientists developed some advanced split window algorithms. In 1995, Becker and Li added water vapor correction to their original split window algorithm in 1990. In 1997, Coll and Caselles developed a new split window algorithm, added water vapor and transmittance correction. Compared to the generalized split window algorithm (based on Becker and Li's 1990 algorithm with no water vapor correction), the retrieved LST bias by using the split window algorithms with water vapor correction is less than the generalized split window algorithm. These algorithms were generally developed for use with AVHRR data and so in the following equations the subscript 4 is for band 4 of AVHRR (10.8µm) and subscript 5 is for band 5 of AVHRR (12µm).

Price's (1984) algorithm:

$$T_{price} = [\,a_0 + a_1(T_4 - T_5)\,]\left(\frac{5.5 - \varepsilon_4}{4.5}\right) + a_3 T_4 \Delta\varepsilon$$

$$\Delta\varepsilon = \varepsilon_4 - \varepsilon_5$$

Vidal's (1991) algorithm:

$$T_{vidal} = a_0 + a_1(T_4 - T_5) + a_2\frac{(1-\varepsilon)}{\varepsilon} + a_3\frac{\Delta\varepsilon}{\varepsilon}$$

$$\varepsilon = \frac{\varepsilon_4 + \varepsilon_5}{2}$$

$$\Delta\varepsilon = \varepsilon_4 - \varepsilon_5.$$

Prata's (1993) algorithm:

$$T_{pra} = \frac{a_0}{\delta}T_4 - \frac{2.42}{\delta}T_5 + d$$

$$\delta = \varepsilon_4 + 2.42\,\tau_5\,\Delta\varepsilon$$

$$d = \left[\frac{1-\delta}{\delta}\right]\left[(B(T_4) - 6)\left(\frac{\partial B_4}{\partial T}\right)^{-1}_{T_4} - T_4\right]$$

Becker and Li's (1995) algorithm:

$$T_{BL} = A_0 + PT^+ + MT^-$$
$$T^+ = \frac{T_4 + T_5}{2}$$
$$T^- = \frac{T_4 - T_5}{2}$$
$$A_0 = a_0 + a_1 W$$
$$P = a_2 + (a_3 + a_4 w \cos\theta)(1-\varepsilon_4) - (a_5 + a_6 W)\Delta\varepsilon$$
$$M = a_7 + a_8 W + (a_9 + a_{10} W)(1-\varepsilon_4) + (a_{11} + a_{12} W)\Delta\varepsilon$$

Coll and Caselles's (1997) algorithm:

$$T_{CC} = a_0 + a_1 T_4 + [(a_2 + a_3(T_4 - T_5)](T_4 - T_5) + \alpha(1-\varepsilon_4) - \beta\Delta\varepsilon$$
$$\varepsilon = \frac{\varepsilon_4 + \varepsilon_5}{2}$$
$$\alpha = (b_4 - b_5)\gamma\tau_5 + b_4$$
$$\beta = \gamma\tau_5 b_5 + \frac{\alpha}{2}$$
$$\gamma = \frac{1-\tau_4}{\tau_4 - \tau_5}$$
$$b_4 = (c_0 + c_1 W)T_4 + (c_2 W + c_3)$$
$$b_5 = (c_4 + c_5 W)T_5 + (c_6 W + c_7)$$

T is the brightness temperature, ε is the surface emissivity, τ is the transmittance. W is the total precipitable water or total column water vapor.

As we can see in some algorithms, the satellite zenith angle at the Earth's surface, the solar zenith angle, and the column water are also included in the regression equation. In the nighttime, the emissivity and brightness temperature at the 3.75 μm band are also used to reduce the measurement uncertainty due to atmospheric correction. Figure 3 shows the summary results for retrieval accuracies and precisions for these candidate LST algorithms.

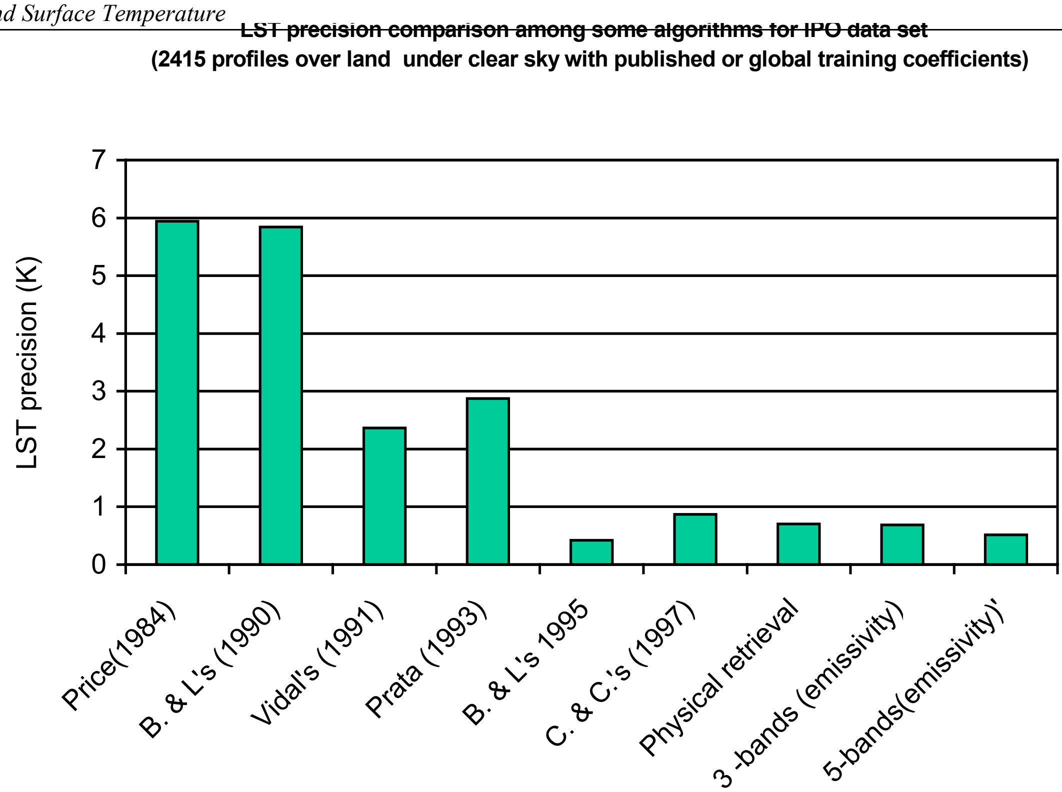

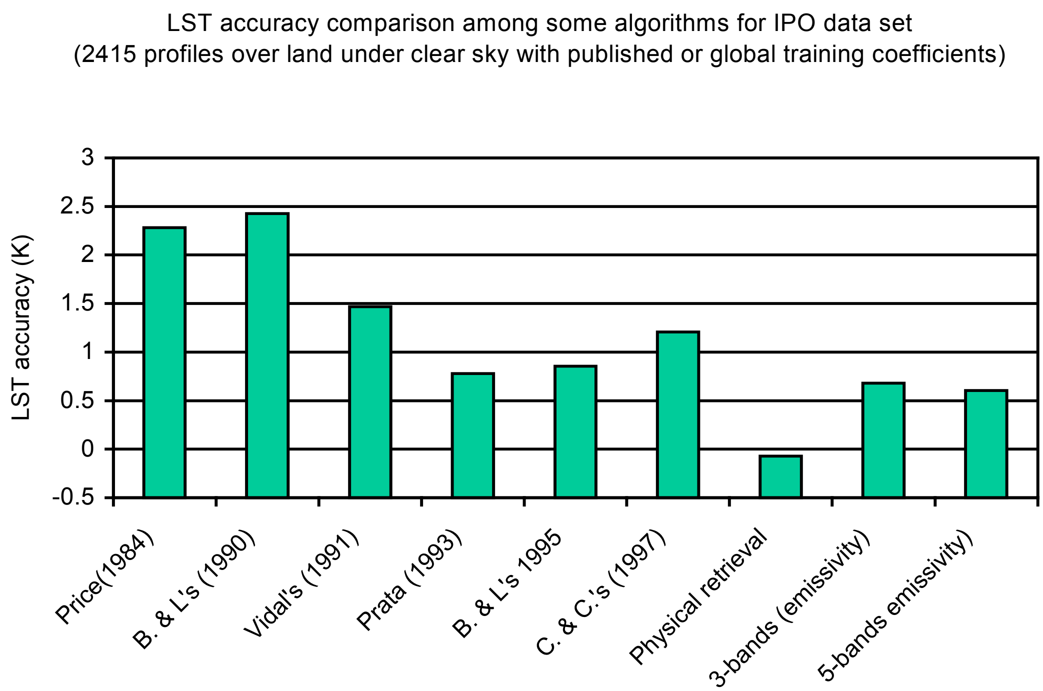

Figure 3. Comparison of different algorithms with IPO 2415 profiles over land under clear condition with the published coefficients or global training coefficients.

3.0 ALGORITHM DESCRIPTION

The cloud cover mask function will be used to eliminate cloud-contaminated or ice-covered pixels. Land cover type and NDVI will be retrieved from visible and near-IR bands. Emissivities of thermal IR bands will be determined using a spectral library. The LST will be calculated using a regression equation. In the baseline algorithm, only land type will be needed. VIIRS Land Cover Type will be used to determine a pixel's type. An equation will then be determined to calculate LST. The backup algorithm is a follow-up of Moderate Resolution Imaging Spectroradiometer (MODIS) algorithm (Wan and Dozier, 1996).

3.1 PROCESSING OUTLINE

The coefficients of regression equations will be obtained using MODTRAN and a global database through our simulation processes. Figure 2a and Figure 2b depict the processing concept for LST retrievals. There are currently two methods. In the first backup algorithm, only one equation is established for the global data (Figure 2a). In the second algorithm, one equation is developed for each land type. There are a total of 21 equations for the global data (Figure 4).

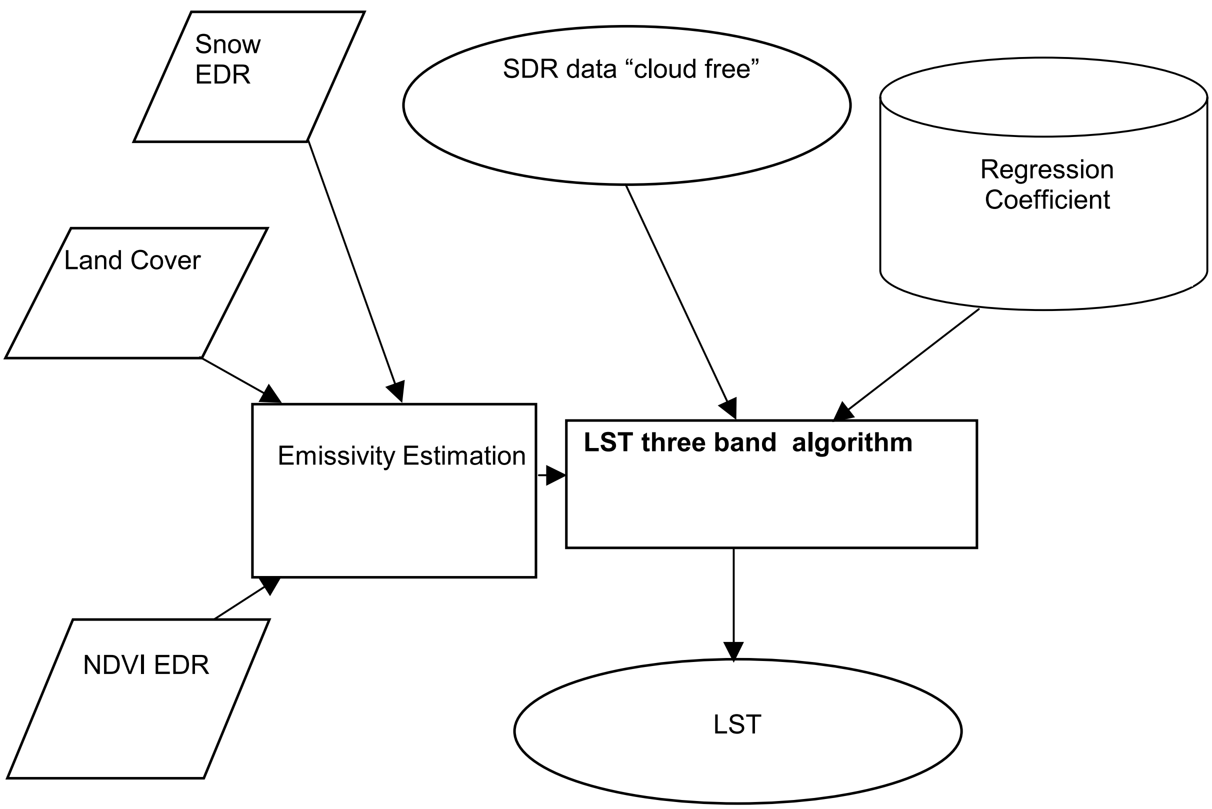

Figure 4a. LST flowchart 1: One equation for all land surface types.

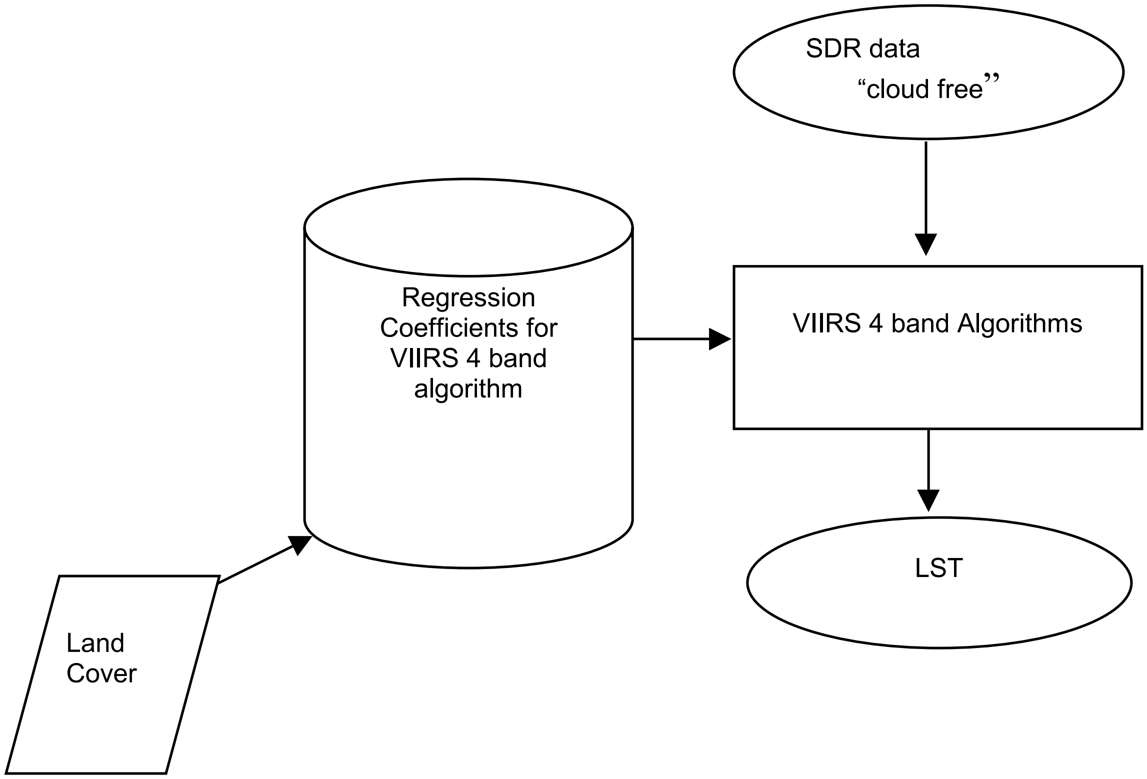

Figure 4b. LST flowchart 2: One equation for each land surface type.

3.2 ALGORITHM INPUT

3.2.1 VIIRS Data

VIIRS inputs required for the LST algorithm are Land Cover classification, and cloud free land IR radiances. For the backup solution, NDVI and Snow Cover EDRs are required.

3.2.2 Non-VIIRS Data

The LST algorithm requires a spectral library. Already available global land surface classification data with 1 km resolution will also be used. A land/ocean mask is needed to determine land pixels.

3.3 THEORETICAL DESCRIPTION OF LAND SURFACE TEMPERATURE RETRIEVAL

3.3.1 Physics of the Problem

In clear sky conditions, the outgoing infrared spectral radiance at the top of atmosphere can be represented by:

$$\begin{aligned} L(\lambda,\mu) = {} & \tau(\lambda,\mu)\varepsilon(\lambda,\mu)B(\lambda,T_s)+L_a(\lambda,\mu)+L_s(\lambda,\mu,\mu_0,\varphi_0) \\ & +L_d(\lambda,\mu,\mu_0,\varphi_0)+L_r(\lambda,\mu,\mu_0,\varphi_0) \end{aligned} \tag{8}$$

Where τ is the transmissivity, ε the surface spectral emissivity, B the Plank function, L_a the thermal path radiance, L_s the path radiance resulting from scattering of solar radiation. L_d is the solar radiance and L_r the solar diffuse radiation and atmospheric thermal radiation reflected by the surface. λ is the wavelength. $\mu = \cos(\theta)$, $\mu_o = \cos(\psi)$, where θ is the satellite zenith angle, ψ the solar zenith angle. φ_o is the azimuth angle.

The wavelength is the wavelength center of a narrow interval because there is no way to measure the exact monochromatic signal as a continuous function of wavelength by satellite sensors. Equation 8 can be used in the 3–14 μm range. It requires complete calculations of the atmospheric radiative transfer to determine the values of all terms on the right side. This equation has been used in many atmospheric radiation models including LOWTRAN (Kneizys *et al*., 1988), MODTRAN (Berk *et al*., 1987), and Moderate Spectral Atmospheric Radiance and Transmittance (MOSART) (Cornette *et al*., 1994).

For far-IR bands, L_d, L_s, and L_r are negligible. Therefore, only the first two terms on the right side of the above equation are important. The first term represents the surface contribution term, and it is the gray-body radiance emitted by the earth's surface. The second term is the atmospheric contribution term, and is the vertically integrated effect of emission from every atmospheric layer modulated by the transmittance of the air above that emitting layer.

$$L(\lambda,\mu) = \varepsilon_0(\lambda,\mu)B(\lambda,T_s)\tau_0(\lambda,\mu) + \int_{\tau_0}^{1} B(\lambda,T_p)\,d\tau(\lambda,\mu,\rho) \tag{9}$$

Where τ_0 is the transmittance at the Earth's surface.

In order to infer the surface information, we should choose window channels with small atmospheric contributions. As shown in Figure 1a, the wavelength between 3.5–4.2 micron, 8–9 micron, and 10–13 micron are some typical atmospheric windows, with less atmospheric absorption. For a perfect window, the total atmospheric transmittance $\tau_0(\lambda\ \mu)$ should be 1.0, the transmittance weighting function should be 0. But as we see from Figure 1b, the transmittances at these windows are not 1.0, this is mainly the result of the water vapor absorption.

In order to see the water vapor's contribution at the atmospheric window channel, we did some simulations to the 2415 profiles offered by the IPO over land surfaces under clear sky conditions by using MODTRAN 3.7. The following five window bands are simulated: 3.75 μm, 10.8 μm (AVHRR channel 4), 12 μm (AVHRR channel 5), and two new VIIRS bands, including 4.005 μm and 8.55 μm.

As we can see from the transmittance vs. surface skin temperature distribution, shown as Figure 5a, at warmer temperatures (285–310 K), for 10.8 and 12 μm channels and the 8.55 μm channel, the transmittances decrease significantly. Most values are below 0.8. This is why most existing split window algorithms using the 11 and 12 μm channels get larger errors in the temperature range 285–310 K. The transmittance for the Shortwave Infrared (SWIR) channel 3.75 μm and 4.005 μm is more stable, with less change to the surface skin temperature; most values are above 0.8. From this aspect, SWIR 3.75 μm and 4.005 μm channels are better window channels than the IR 11, 12, and 8.55 micron channels. The most stable channel is at 4.005 microns. From the transmittance vs. total column water vapor (Figure 5b), we can also see that the transmittance at the 4.005 micron channel is the most stable. It changes very little with the column water vapor amount. While the transmittance at 3.75 micron channel has a linear relationship with the precipitable water, the transmittances at 11, 12, and 8.55 microns decrease significantly as the water vapor increases and the relationship is also not linear. The information from SWIR window channel can be used when we retrieve warmer surface temperatures.

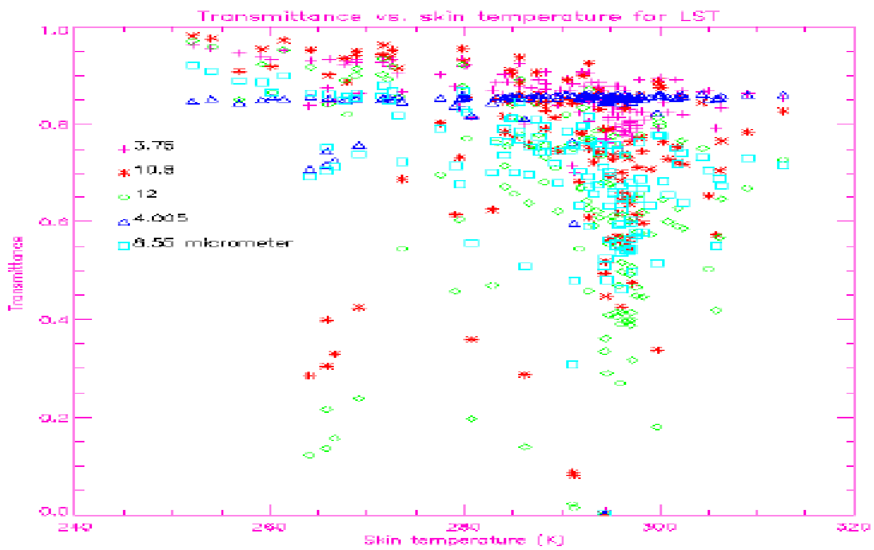

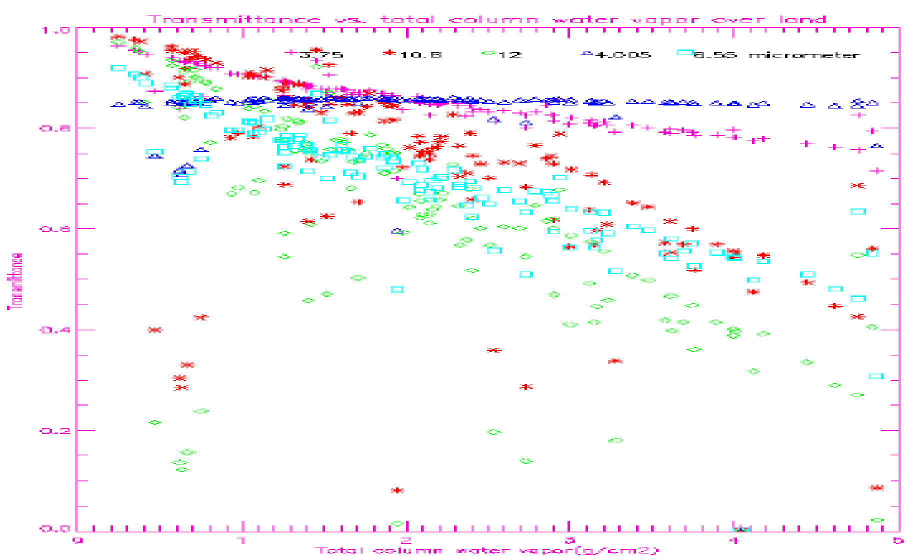

Figure 5a. Upper Panel: Transmittance vs. LST. 5b. Lower Panel: Transmittance vs. total column water vapor over land.

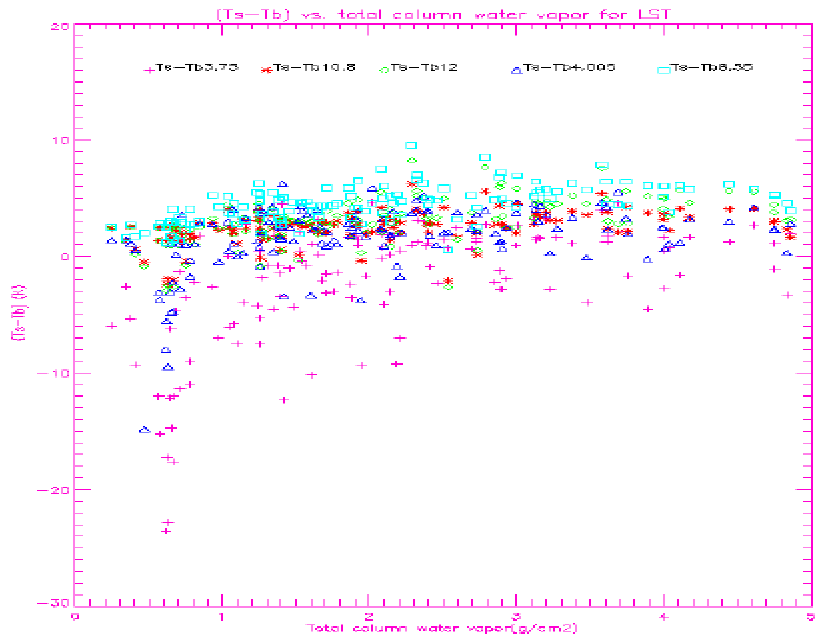

Figure 5c. Temperature deficits (T_s-T_b) vs. total column water vapor distribution.

From the difference between the surface temperature and brightness temperature vs. precipitable water distribution, as shown in Figure 5c, the temperature deficit (T_s-T_b) at IR window channels 11, 12, and 8.55 microns is very stable, while the surface temperature at SWIR channels 3.75 and 4.005 microns can be much lower than the brightness temperature, sometimes by more than 10 degrees. This is because in the daytime, the SWIR channel contains both reflected solar radiation and radiation emitted by the surface and the atmosphere, this is the so-called solar glint. So the best way to retrieve surface temperature is to appropriately combine IR and SWIR window channels.

Currently, most existing LST algorithms are variants based on Becker and Li's split window technique (1990).

$$Ts = (A1 + A2\frac{1-\varepsilon}{\varepsilon} + A3\frac{\Delta\varepsilon}{\varepsilon^2})\frac{T_{11}+T_{12}}{2} + (B1 + B2\frac{1-\varepsilon}{\varepsilon^2} + B3\frac{\Delta\varepsilon}{\varepsilon^2})(T_{11} - T_{12}) + C \qquad (10)$$

Where $\varepsilon = (\varepsilon_{11} + \varepsilon_{12})/2$ and $\Delta\varepsilon = \varepsilon_{11} - \varepsilon_{12}$. ε_{11} and ε_{12} are the emissivities at 10.8 µm and 12 µm bands respectively. T_{11} and T_{12} are the brightness temperatures at 10.8 µm and 12 µm bands respectively.

One of the major difficulties in the development of the LST algorithm is the considerable spectral variation in emissivities for different land surface types. Observation of emissivity spectra shows that in general, emissivity spectra with high values exhibit little variation, while those with lower values exhibit a greater variation, such as grass, as shown in Figure 6.

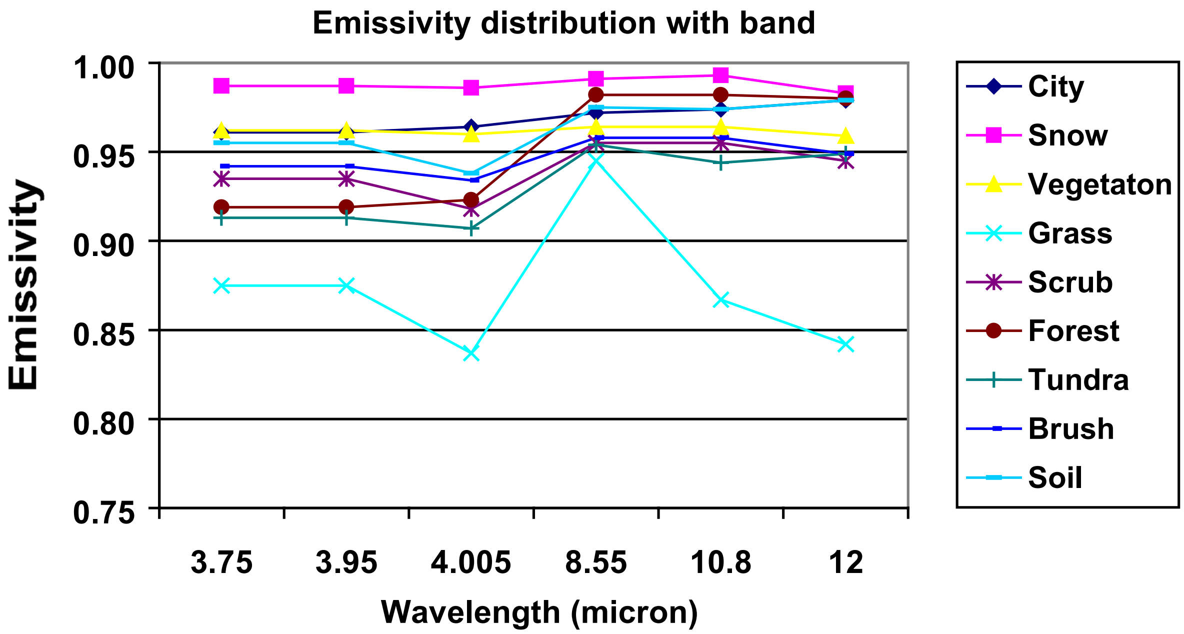

Figure 6. Variation in emissivity for different surface types.

If we ignore the change of emissivity for a certain land surface type, the radiance error introduced by the atmosphere ΔL can be represented by:

$$\begin{aligned}\Delta L &= B(\lambda,T_s) - L(\lambda,\mu) = B(\lambda,T_s) - \tau(\lambda,\mu)B(\lambda,T_s) - L_a(\lambda,\mu) \\ &= -\int_1^{\tau(\lambda,\mu)} B(\lambda,T_s)d\tau(\lambda,\mu,p) + \int_1^{\tau(\lambda,\mu)} B(\lambda,T_p)d\tau(\lambda,\mu,p) \\ &= -\int_1^{\tau(\lambda,\mu)} (B(\lambda,T_s) - B(\lambda,T_p))d\tau(\lambda,\mu,p)\end{aligned} \tag{11}$$

From the Planck function we find:

$$\Delta L = \frac{\partial B}{\partial T}\Delta T = \frac{\partial B}{\partial T}(T_s - T_\lambda) \tag{12}$$

For an optically thin gas the following approximations can be made:

$$d\tau = d\{\exp(-k_\lambda L)\} = -k_\lambda dl \tag{13}$$

where k_λ is the absorption coefficient and l is the optical path-length. If we assume that the Planck function is adequately represented by a first order Taylor series expansion in each channel window, then:

$$B(\lambda,T_s)-B(\lambda,T_p)=\left.\frac{\partial B(\lambda,T_p)}{\partial T}\right|_{T_s}(T_p-T_s) \tag{14}$$

Substituting Equations 12, 13, 14 into Equation 11, we obtain:

$$T_s-T_\lambda=k_\lambda\int_1^\tau (T_s-T_p)dl \tag{15}$$

Therefore, if we select two spectral regions of the atmosphere, we will have two linear equations with different k_λ to solve simultaneously.

For example if we consider the two channels as λ=1 and λ=2, then we get:

$$T_s-T_1=-(T_2-T_1)k_1/(k_2-k_1) \tag{16}$$

This equation is similar to the Sea Surface Temperature (SST) equation, but can only be used for one land type, assuming the band emissivity does not vary within this land type. Figure 7a shows the relationship between band temperature deficits T_s-T_{11} and T_s-T_{12} for forests. The data are global data with 17,885 skin temperatures and atmospheric profiles. The relationship is rather linear, which confirms that for a particular land type, the linear split window algorithm used in SST retrieval can be adopted for LST. Figure 7b is similar to Figure 7a, but for simulations of 23 land cover types. There is much more variation in this figure; the relationship is not linear. Emissivities, therefore, have to be considered as an important factor for Becker and Li's 1990 LST algorithm.

For land surfaces, the emissivity for each channel changes with surface type. Table 3 shows the band-averaged emissivities for 23 surface types derived from MOSART spectra. Although this table contains a majority of the NPOESS land surface types, the full spectral library for NPOESS land surface types is under development. The differences between 10.8 µm and 12 µm bands are small for most of the types, thus making the VIIRS land surface separated algorithm feasible.

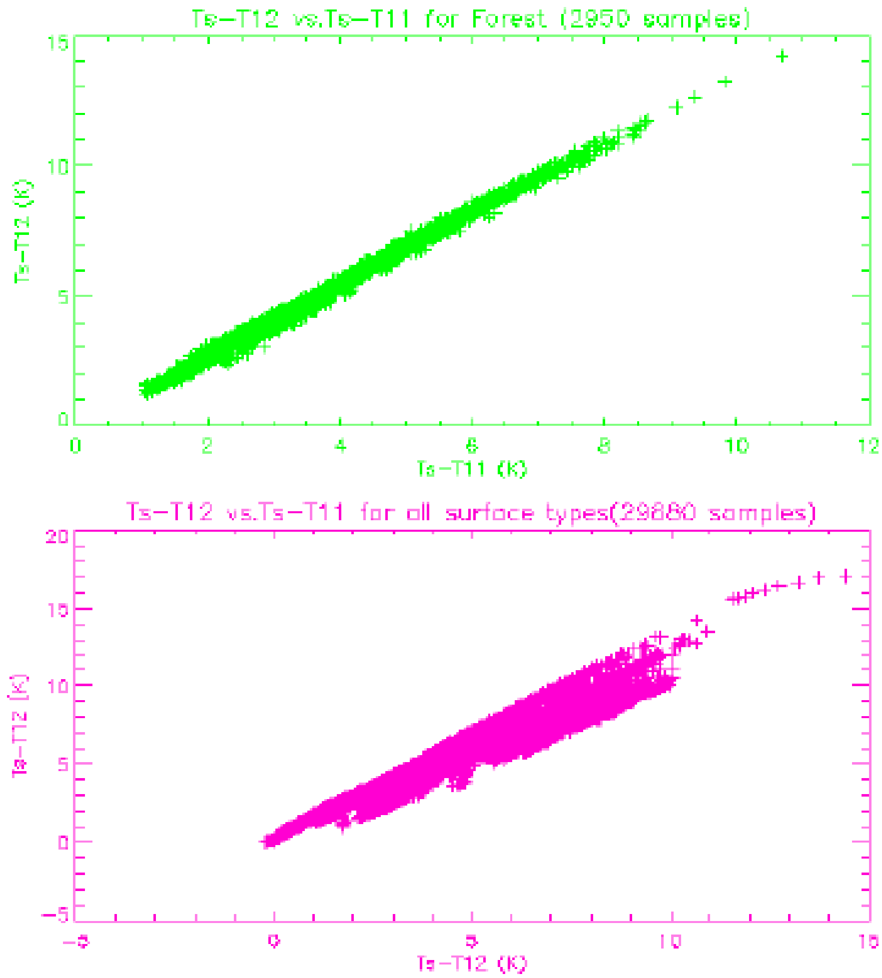

Figure 7. (Upper panel) Relationship between temperature deficits of 10.8 µm and 12 µm bands for forest only. (Bottom panel) Relationship between temperature deficits of 10.8 µm and 12 µm bands for all 23 land types.

Table 3. Band-Averaged Emissivities of 23 Surface Types in VIIRS Bands 10, 11, 12, SST1, SST2, SST4.

Surface Type Index	Type of Materials	$\varepsilon_{3.75}$	$\varepsilon_{10.8}$	ε_{12}	$\varepsilon_{3.99}$	$\varepsilon_{4.00}$	$\varepsilon_{8.55}$
1	Water	0.980	0.990	0.990	0.980	0.980	0.985
2	Old snow	0.987	0.993	0.983	0.987	0.986	0.991
3	Sea ice	0.987	0.995	0.983	0.987	0.982	0.992
4	Compacted soil	0.930	0.957	0.967	0.930	0.895	0.965
5	Tilled soil	0.951	0.970	0.977	0.951	0.926	0.975
6	Sand	0.500	0.950	0.980	0.500	0.550	0.900
7	Rock	0.800	0.915	0.960	0.800	0.840	0.895
8	Cropland	0.962	0.964	0.959	0.962	0.960	0.964
9	Meadow grass	0.875	0.867	0.842	0.875	0.837	0.945
10	Scrub	0.935	0.955	0.945	0.935	0.918	0.955
11	Broadleaf forest	0.952	0.962	0.956	0.952	0.957	0.962
12	Pine forest	0.905	0.990	0.990	0.905	0.907	0.990
13	Tundra	0.913	0.944	0.949	0.913	0.907	0.954
14	Grass-soil	0.908	0.921	0.918	0.908	0.872	0.957
15	Broadleaf-pine forest	0.919	0.982	0.980	0.919	0.923	0.982
16	Grass-scrub	0.905	0.911	0.893	0.905	0.877	0.950
17	Soil-grass-scrub	0.915	0.929	0.923	0.915	0.885	0.956
18	City	0.961	0.974	0.979	0.961	0.964	0.972
19	Pine-brush	0.920	0.973	0.967	0.920	0.913	0.973
20	Broadleaf-brush	0.942	0.958	0.949	0.942	0.934	0.958
21	Wet soil	0.955	0.974	0.979	0.955	0.938	0.975
22	Scrub-soil	0.932	0.956	0.959	0.932	0.904	0.961
23	Broadleaf (70%)—Pine (30%)	0.938	0.970	0.966	0.938	0.942	0.970

Figure 8 shows the emissivity change as a function of surface types for five VIIRS mid-IR and far-IR bands. Far-IR band emissivities are relatively stable for all land types. The changes of mid-IR emissivity are larger at land type 6 (sand) and type 7 (rock).

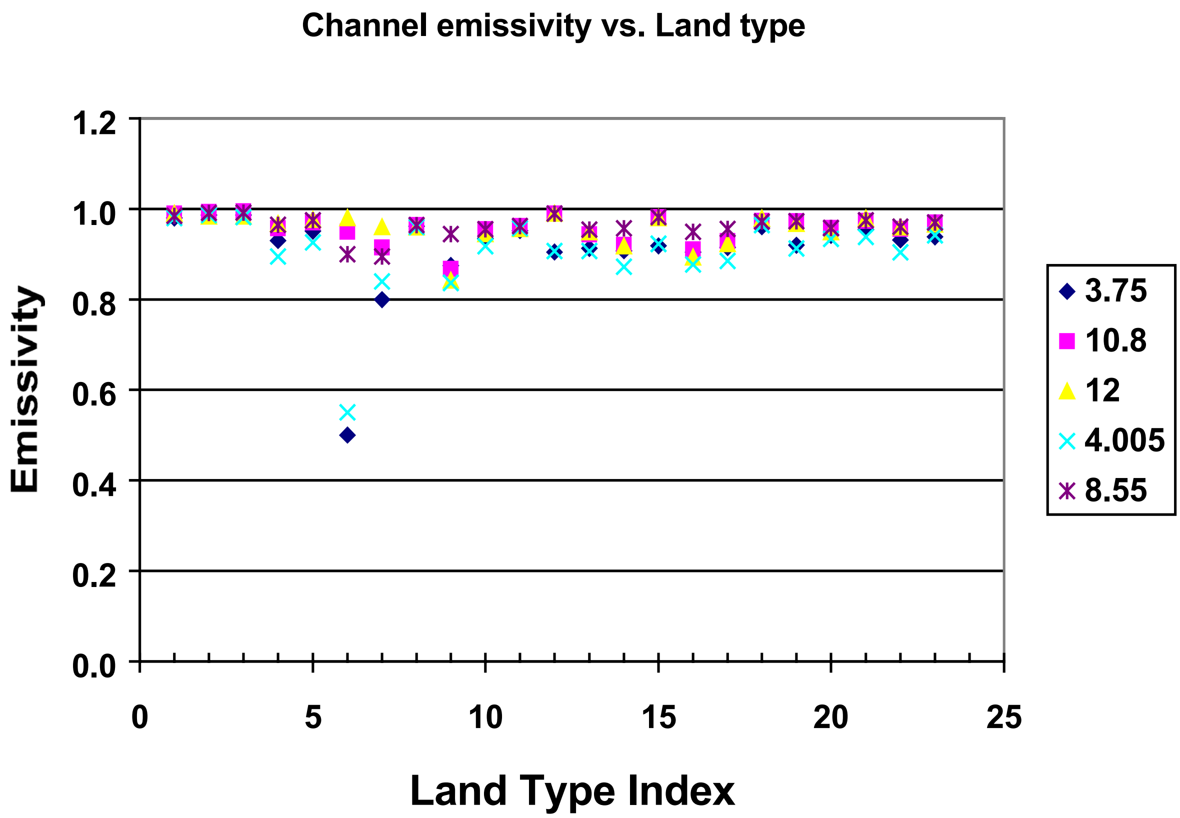

Figure 8. Channel emissivities for 23 land types.

In general, Equation 15 can be written as:

$$\boldsymbol{T}_s = \boldsymbol{C}\boldsymbol{T}_b$$

The coefficient vector $\boldsymbol{C}$, relating observed brightness temperatures to LST, is determined using a regression method by solving:

$$\boldsymbol{C} = \boldsymbol{Y}\boldsymbol{X}^T(\boldsymbol{X}\boldsymbol{X}^T)^{-1} \quad (17)$$

The $\boldsymbol{Y}$ matrix contains a large number of training LSTs and the $\boldsymbol{X}$ matrix contains brightness temperatures from VIIRS far-IR and mid-IR channels. In general, the $\boldsymbol{X}$ matrix may include non-linear terms.

Currently, the LST uncertainty from the regression algorithm is about 1 ~ 3 K.

3.3.2 Mathematical Description of the Algorithm

Based on the previous section's discussion of the physics of the problem, the mathematical descriptions of the algorithm can be simply stated.

Baseline Algorithm

VIIRS-4 band day/night LST algorithm establishes one equation to each surface type by using 4 VIIRS bands (10.8, 12, 3.75, and 4.005 μm), and it added a solar zenith angle correction during the daytime:

Daytime:

$$LST_i = a_0(i) + a_1(i)T_{11} + a_2(T_{11} - T_{12}) + a_3(i)(\sec\theta - 1) + a_4(i)T_{3.75} + a_5(i)T_{4.0} + a_6(i)T_{3.75}\cos\varphi \\ + a_7(i)T_{4.0}\cos\varphi + a_9(i)(T_{11} - T_{12})^2 \qquad i = 1,\ 23 \tag{18}$$

Nighttime or day and night:

$$LST_i = b_0(i) + b_1(i)T_{11} + b_2(T_{11} - T_{12}) + b_3(i)(\sec\theta - 1) + b_4(i)T_{3.75} + b_5(i)T_{4.0} + b_6(i)T_{3.75}{}^2 \\ + b_7(i)T_{4.0}{}^2 + b_9(i)(T_{11} - T_{12})^2 \qquad i = 1,\ 23 \tag{19}$$

Where i is the index of 23 VIIRS surface types.

Without the solar zenith angle correction, Equation 19 is used for both day and nighttime.

Backup Algorithm:

Three band Split Window: (10.8, 12, 8.55 μm bands*)*

$$T_S = a_0 + a_1\frac{(1-\varepsilon_{10.8})}{\varepsilon_{10.8}}T_{10.8} + a_2\frac{(1-\varepsilon_{12})}{\varepsilon_{12}}T_{12} + a_3\frac{(1-\varepsilon_{8.55})}{\varepsilon_{8.55}}T_{8.55} + a_4(\sec\theta - 1) \tag{20}$$

3.3.3 Test Data Set Description

The Test Data Sets we used to test our algorithms during Phase I include:
- IPO simulated scenes: TERCATS
- National Center for Environmental Prediction (NCEP) global snapshot surface temperature data set with matching atmospheric profiles at the resolution 2.5 x 2.5 degrees;
- 8344 profiles offered by IPO with matching surface skin temperature;
- NASA/NOAA pathfinder land data set with 8-km resolution.

IPO simulated scene: TERCATS

One important data set we used to test LST algorithms was the IPO-simulated scenes. The IPO provided land cover images at different locations and with different resolutions. We then found the matched surface reflectance for the simulated bands from our spectral databases, and performed sensor and view geometry calculations, with appropriate surface truth. The MODTRAN 3.7 radiative transfer code was used to derive simulated top-of-the-atmosphere (TOA) radiance in different bands. The Santa Barbara Remote Sensing (SBRS) noise models, Modulation Transfer Function (MTF) model and calibration errors were applied to the TOA radiances. We performed many tests on the different IPO scenes. The following is a discussion of these tests and their results.

Figure 9 shows the IPO Tercat scene at 50m resolution. The truth LST for this scene is shown as the upper panel of Figure 10. Most currently used algorithms are based on Becker and Li's 1990 algorithm. Figure 10 lower panel is the retrieved LST distribution by using this split window algorithm. As we can see most of the retrieved land surface temperature are colder than the truth LST. From the retrieved precision distribution, shown as Figure 11, we can clearly see that most biases are negative. This is because the truth LST for this scene is a warm temperature and most temperature values are above 296K. As we discussed before, split window algorithms by using 11 and 12 μm get bigger errors at warmer temperatures. Figure 12 shows the precision distribution vs. temperature, we can see that the split window algorithm can't meet the threshold requirement 0.5K for temperatures above 293 K.

NCEP global snapshot surface temperature data set

The global snapshot surface temperature data set is at 2.5^{o} by 2.5^{o} resolution supplied by the National Centers for Environment Prediction (NCEP), with matching atmospheric profiles. The upper panel in Figure 13 shows the LST distribution for the global data set at 00 Z, July 1, 1993. The middle panel shows the retrieved LST with the generalized split window algorithm for the case of baseline sensor noise. The lower panel is the difference. The temperature range is from 210 to 315 K, the precision is 0.73 K and the maximum error is 3.58 K.

AVHRR Pathfinder TDS

Another data set used is a surface temperature scene at 1-km resolution derived from Advanced Very High-Resolution Radiometer (AVHRR) 1b data. These data were used to simulate the top-of-atmospheric radiance (TOA) with MODTRAN. The Santa Barbara Remote Sensing (SBRS) sensor noise models were applied to the TOA radiance. Both noise-free TOA radiance and noisy TOA radiance were used to retrieve LST.

3.3.4 Variance and Uncertainty Estimates

There are mainly three geophysical factors that contribute to the uncertainty of satellite LST retrieval: land surface classification, emissivity determination errors and atmospheric correction errors. In addition sensor errors need to be accounted for.

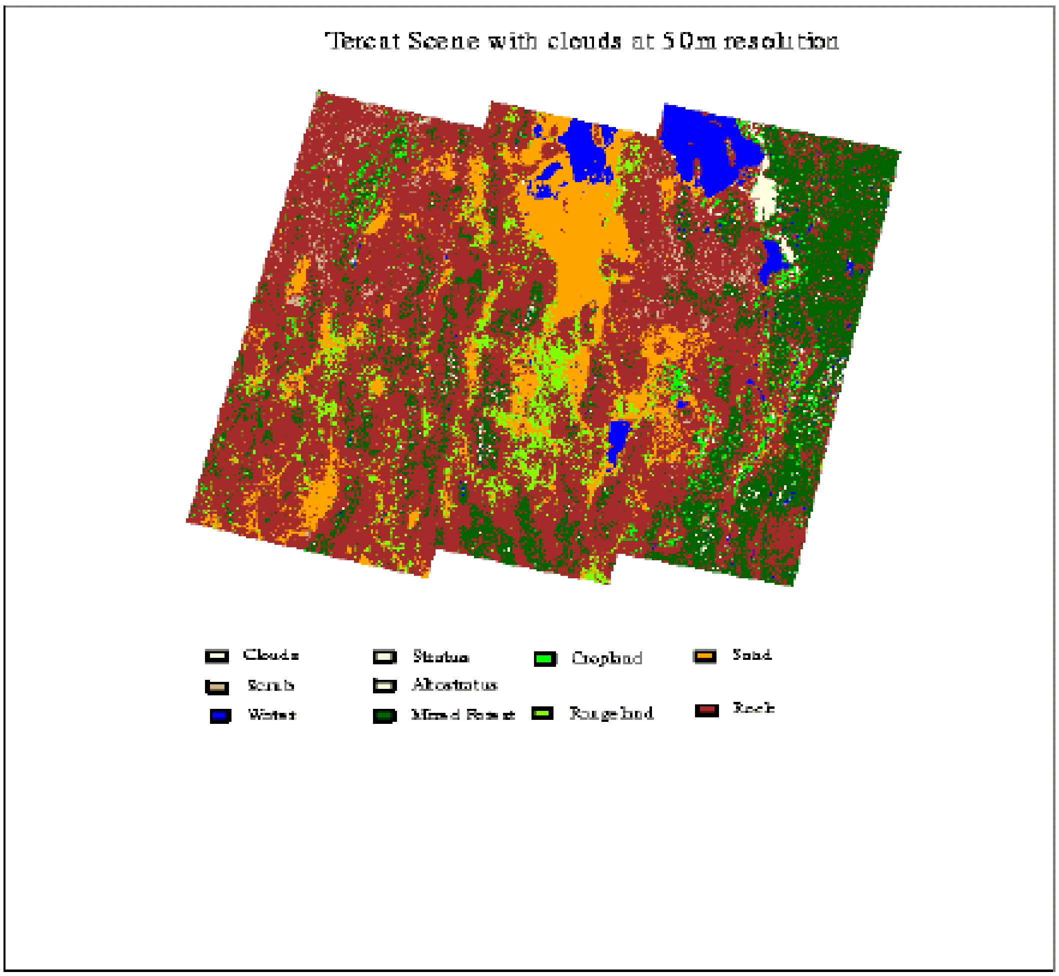

Figure 9. IPO Tercat scene at 50m resolution.

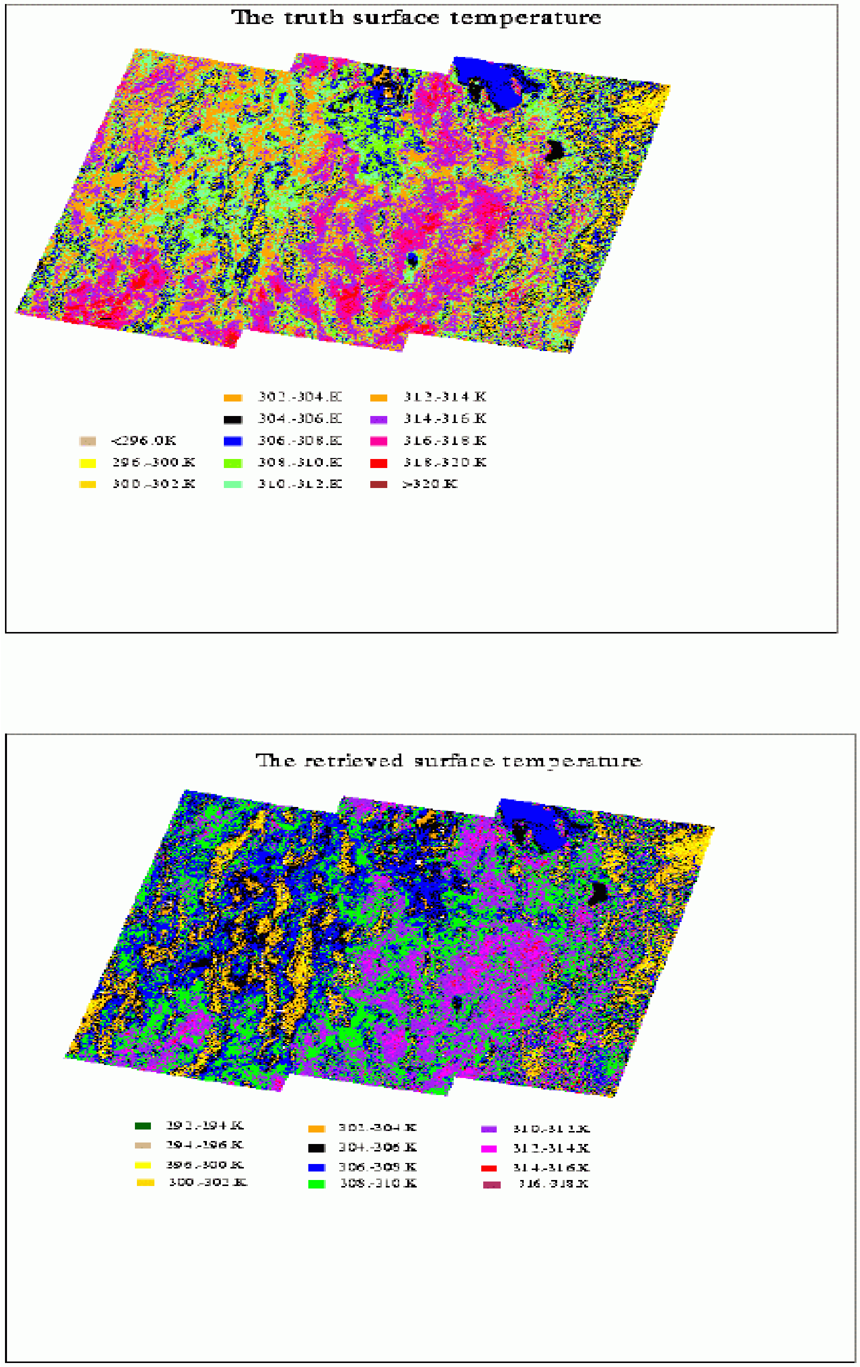

Figure 10. Truth land surface temperature for IPO 50 m Tercat scene (upper panel); retrieved LST distribution by using generalized split window algorithm (bottom panel).

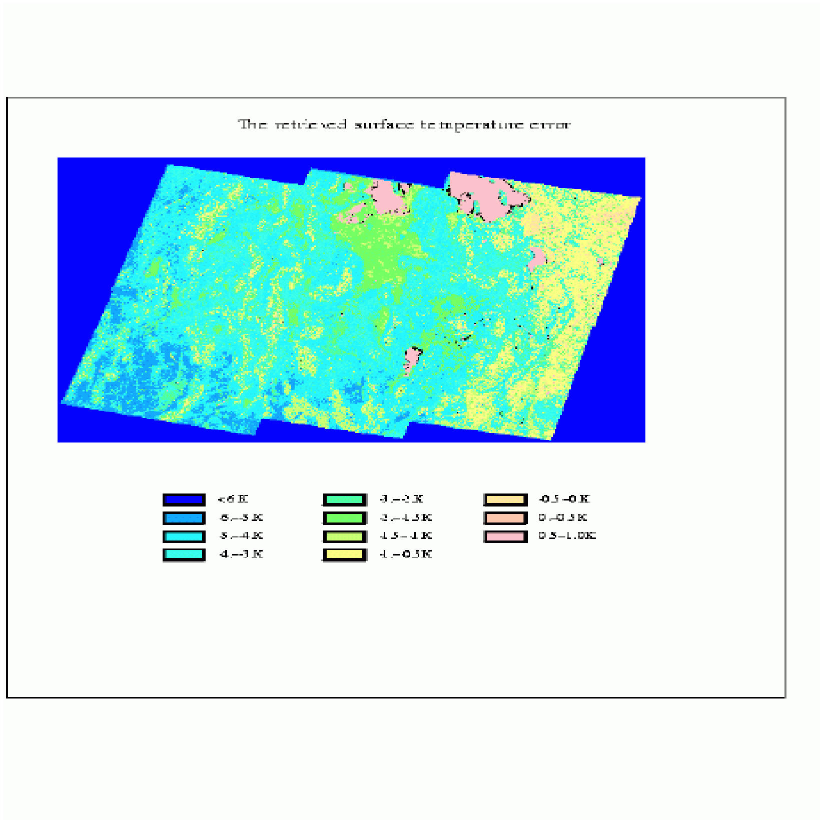

Figure 11. LST retrieval bias distribution by using generalized split window algorithm.

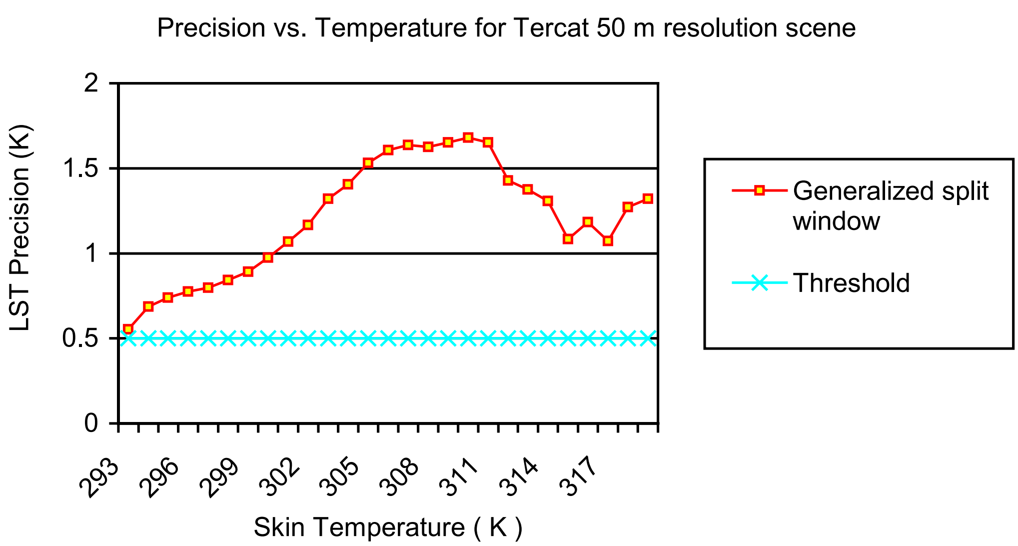

Figure 12. Precision vs. temperature distribution for IPO 50 m Tercat scene.

Emissivity approach

Figure 14 shows the LST retrieval error vs. temperature distribution. The upper panel is for generalized split window algorithm. As we can see the generalized split window by using 11 and 12 µm bands has bigger errors at warmer temperature between 280-310K.The second panel is VIIRS-3 bands algorithm with the combination of 11, 12 µm bands with 3.75 µm band. The third is for combination of 11,12 µm with 4.005µm band. The bottom panel is for combination of 11, 12 with 8.55 µm. VIIRS-three band algorithm by combining 11 and 12 µm with 8.55 µm gives the best result (VIIRS backup solution).

Although the 3 band algorithm by combining 11, 12 µm, and the 8.55 µm band gave a better result than the generalized split window, it still shows a bigger error at warmer temperature between 295~305 K. At cold temperatures below 225 K, it is worse than the generalized split window. If we separate the whole temperature range into two categories below 285 K and above 285 K, the result is shown in Figure 15. Here the precision at cold temperatures below 285 K can meet the threshold 0.5 K, it is only about 0.25 K, the precision became much better at warmer temperature too.

Land cover approach

For a specific surface type, the deficits between the surface temperature and the brightness temperature at 11 µm and 12 µm have very good linear relationship, therefore split window algorithms can be adopted to a specific surface type. Land Cover Maps exist and will be improved during the MODIS era, Figure 16. For each surface type, we establish one set of regression coefficients between the surface temperature and 11µm and 12 µm brightness temperature. Figure 17a displays the LST precision for different land surface types. The upper line represents the result derived from the generalized split window algorithm. The other lines present the results from the VIIRS split window algorithm for various land surface types. This figure shows that the Land Cover method can improve the retrieval precision for all surface types. Figure 17b shows the summary statistics of retrieval for all the surface types vs. different sensor noise model. The VIIRS Land Cover specific split window method shows better precision than that of the generalized split-window algorithm. The sensor noise level specification is equivalent to noise model 3.

Figure 18 shows the utility of a solar zenith correction function being added to the equation during daytime retrievals. The solar zenith correction is particularly useful at higher temperatures. Figures 19 and 20 show the estimated performances of the baseline algorithm as a function pf view angle and temperature for both day and night respectively.

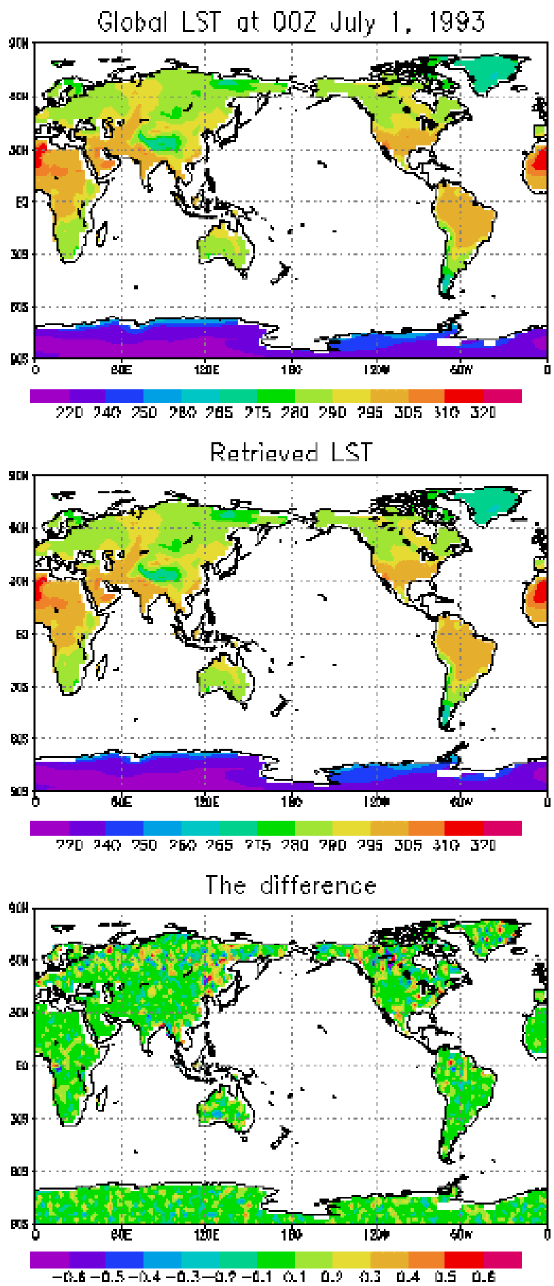

Figure 13. Upper panel: Global LST. Middle panel: Retrieved LST. Lower panel: The difference between the LST values.

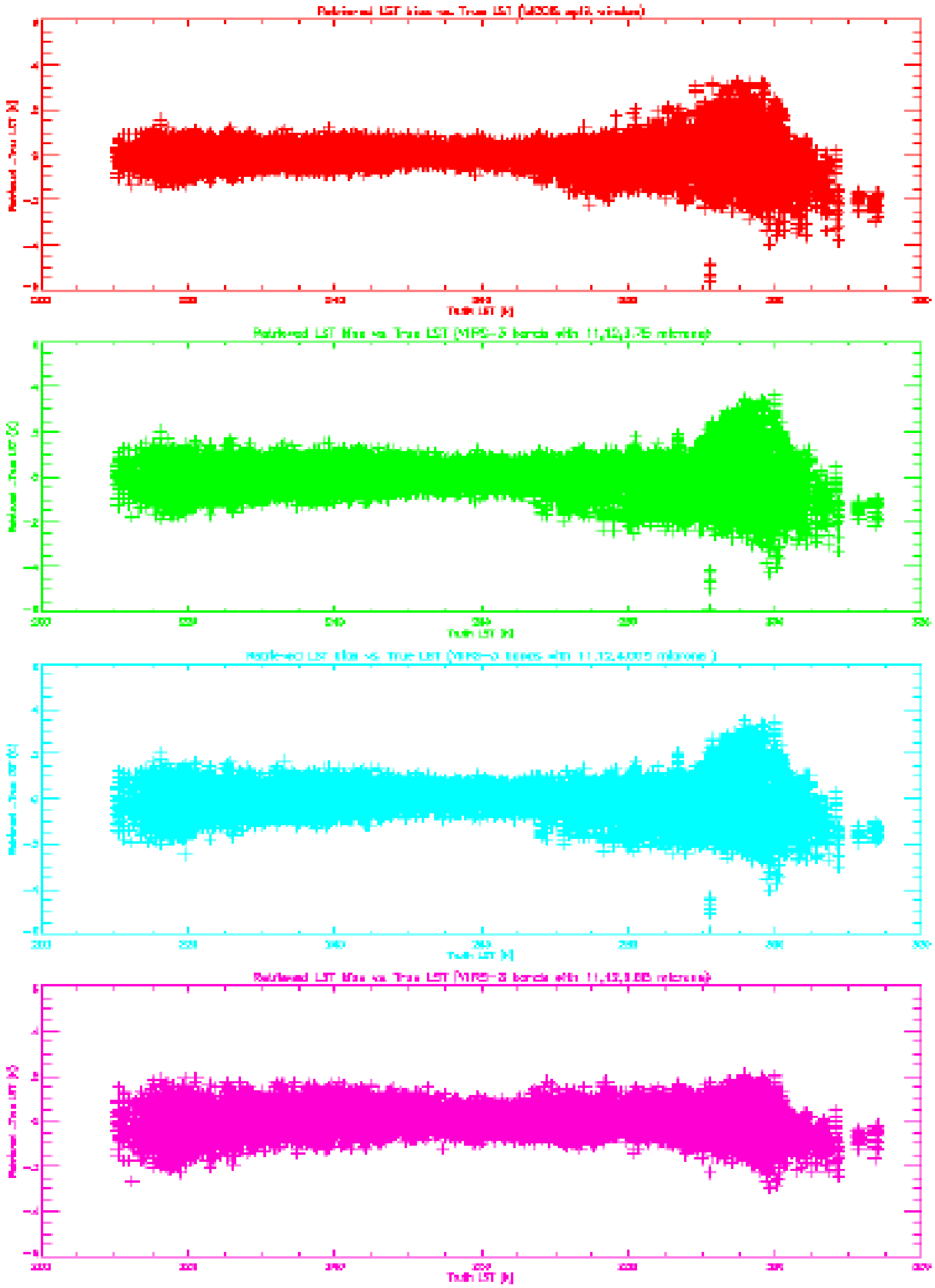

Figure 14. LST retrieval error vs. temperature distribution for different band combinations, compared with generalized split window. The upper panel: generalized split window. The second: 11,12 and 3.75 µm. The third: 11, 12 and 4.005 µm. The bottom: 11, 12 and 8.55 µm.

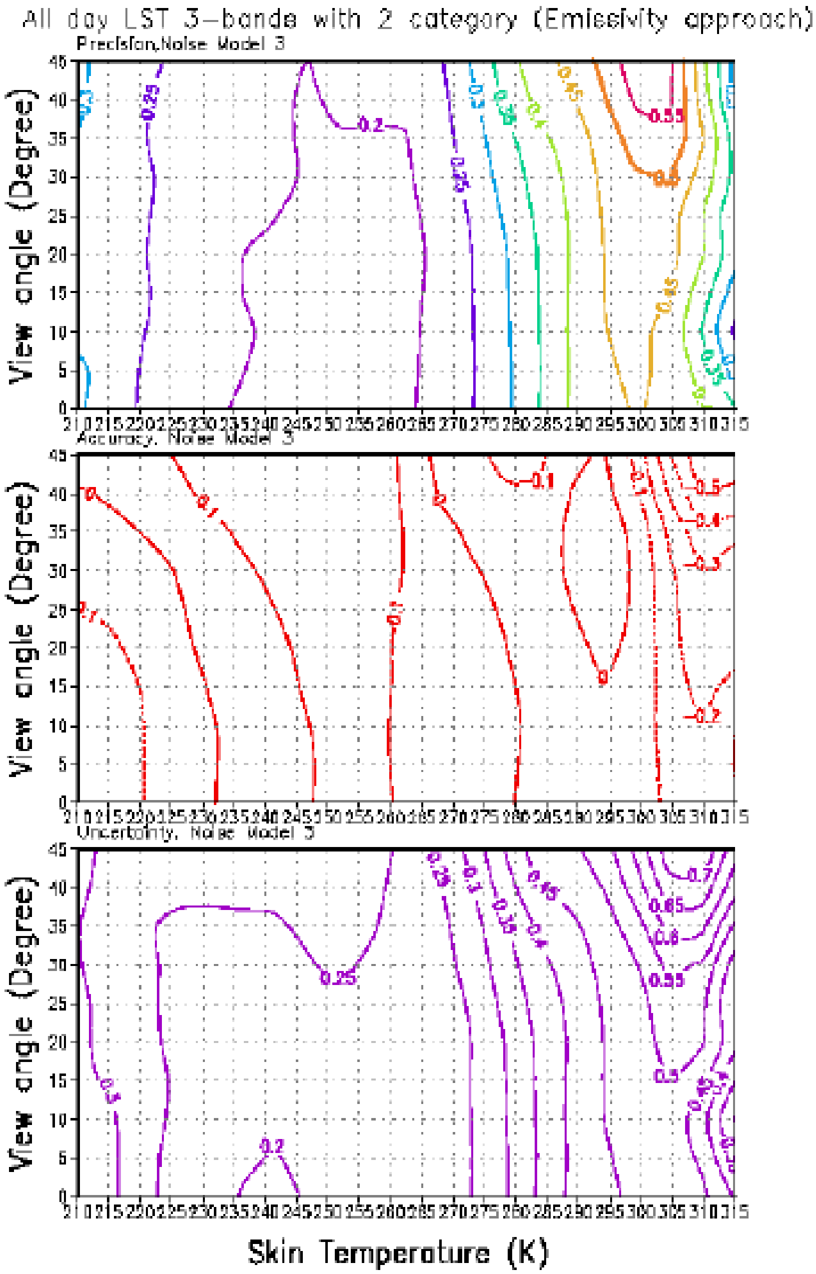

Figure 15. LST precision (upper panel), accuracy (middle) and uncertainty (bottom) distribution vs. satellite view angle and LST for 3-band algorithm (emissivity approach) with two temperature categories (below 285 K) and above 285 K.

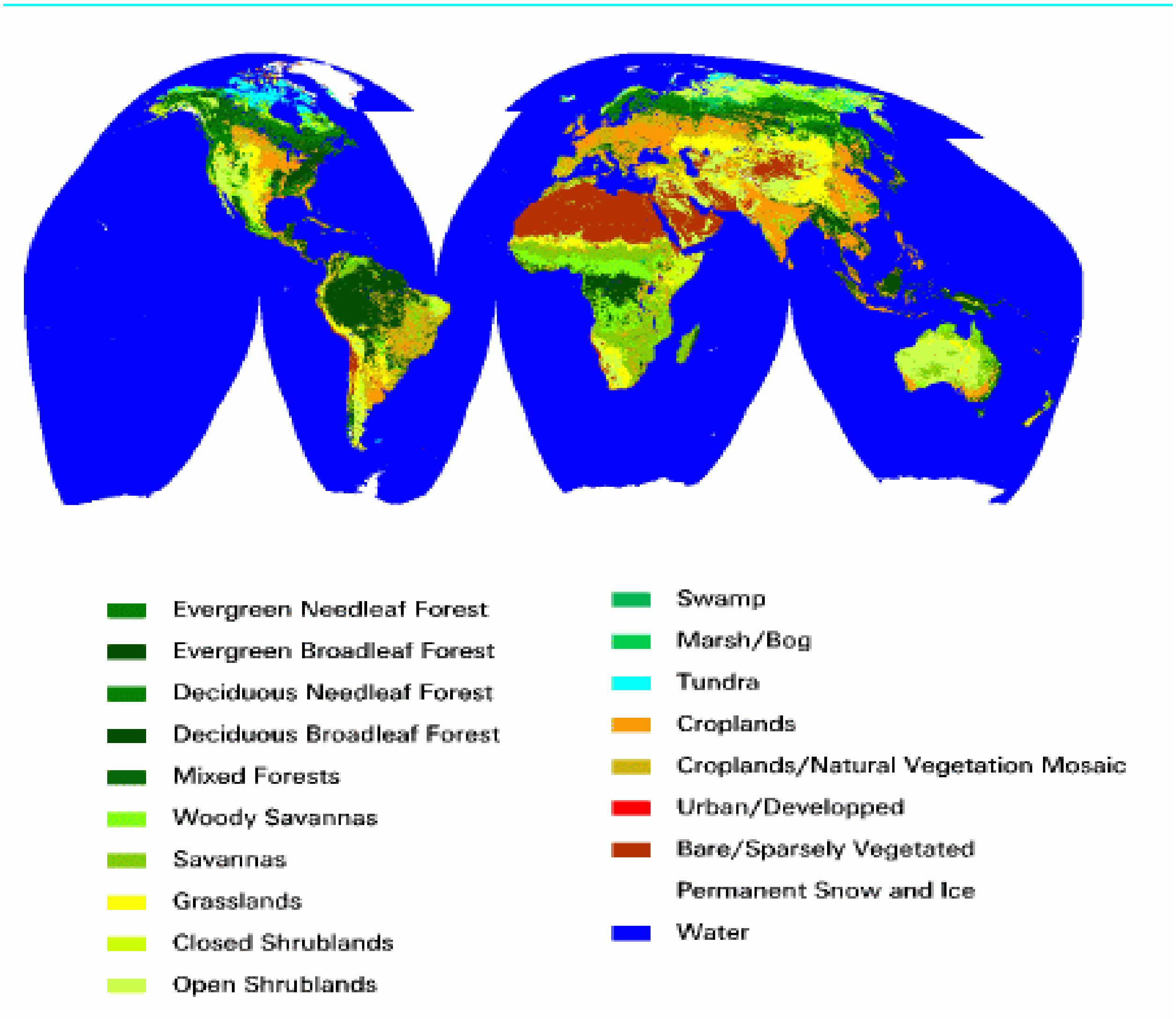

Figure 16. Global land cover distribution at 8km resolution in July 1992.

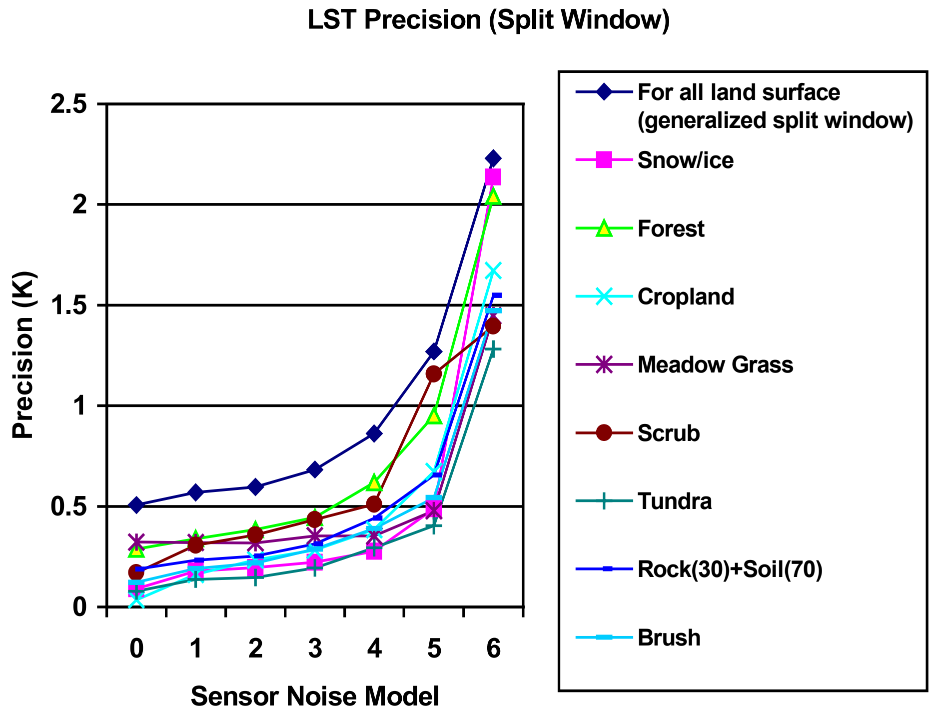

Figure 17a. Precision analysis for the two different retrieval methods.

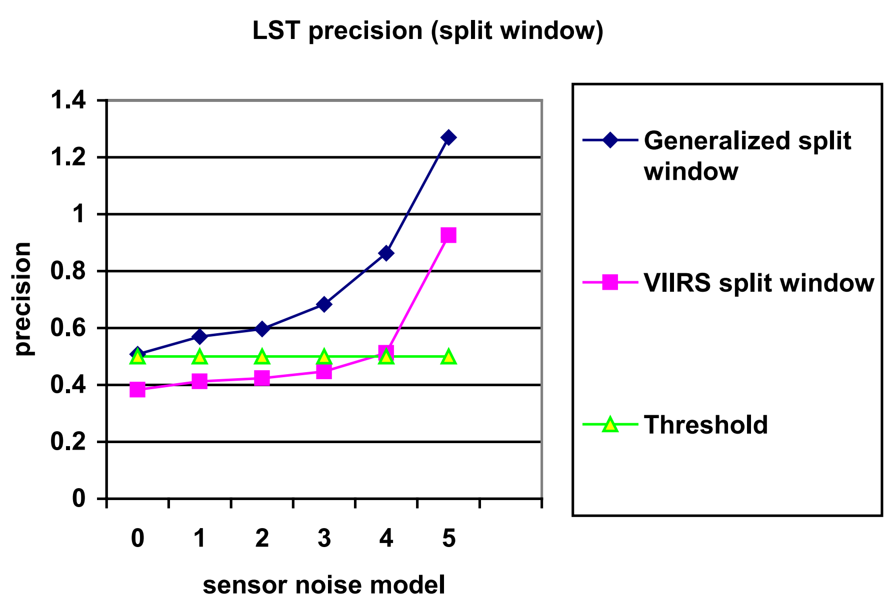

Figure 17b. Global LST retrieval precision from the two retrieval methods.

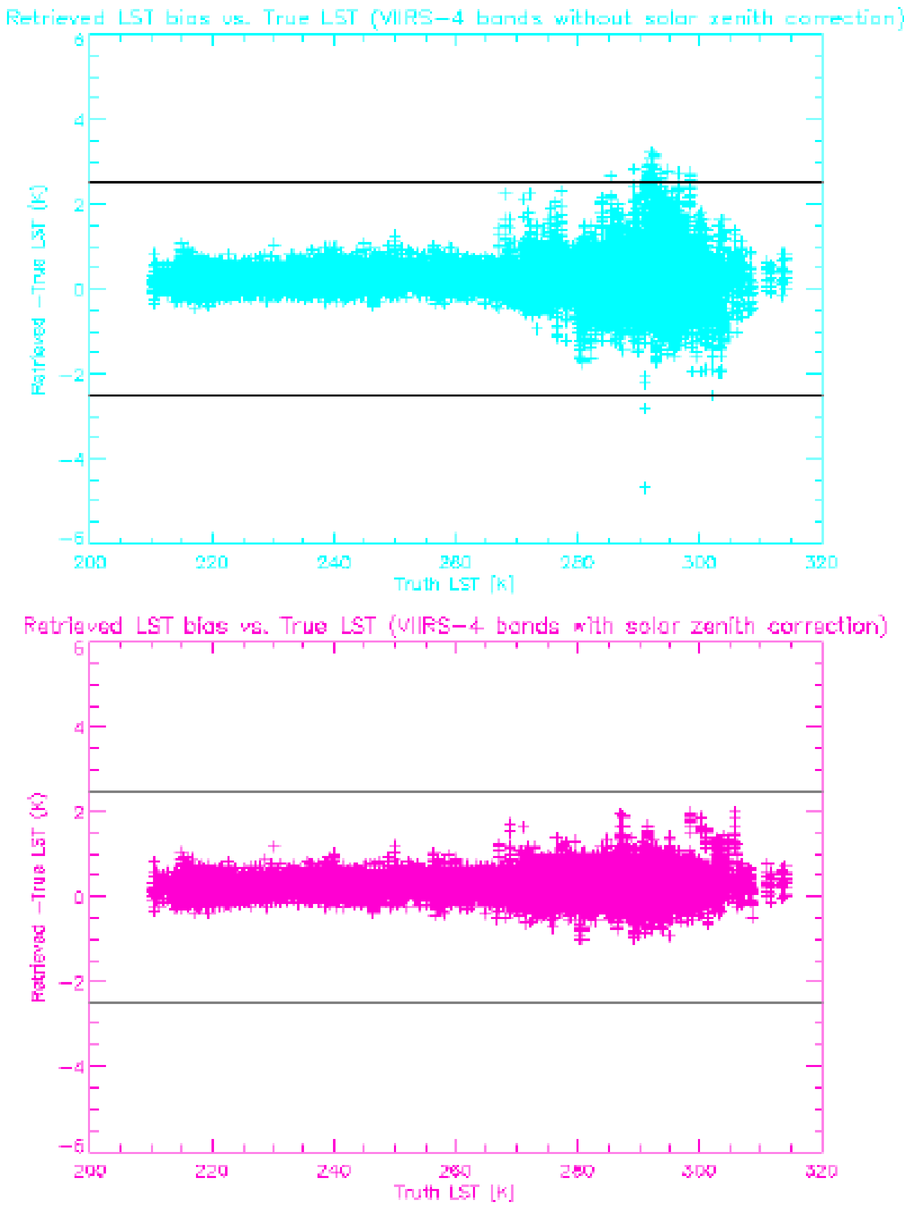

Figure 18. LST retrieval error vs. LST distribution for VIIRS–4 bands algorithm. The upper panel: Without solar zenith angle correction. The bottom panel: With solar zenith angle correction during the daytime.

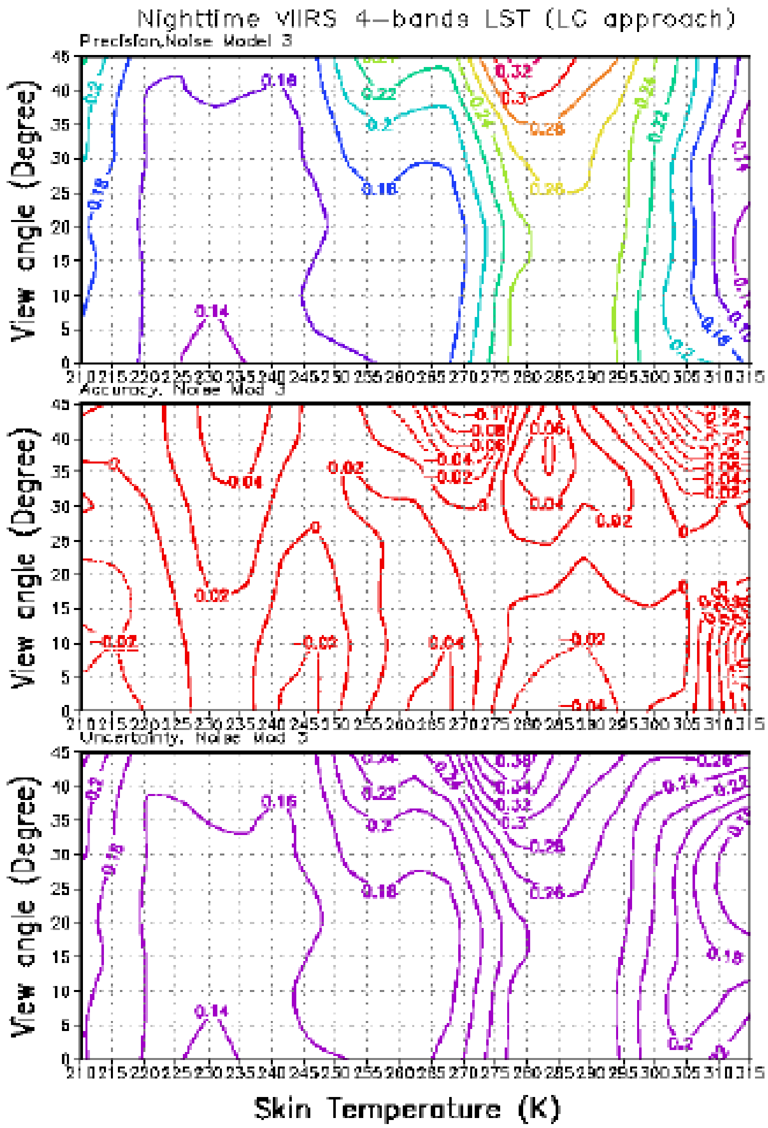

Figure 19. Nighttime LST precision (upper panel), accuracy (middle) and uncertainty (bottom) distribution over satellite view angle and LST by using VIIRS-4 band algorithm (LC approach) .

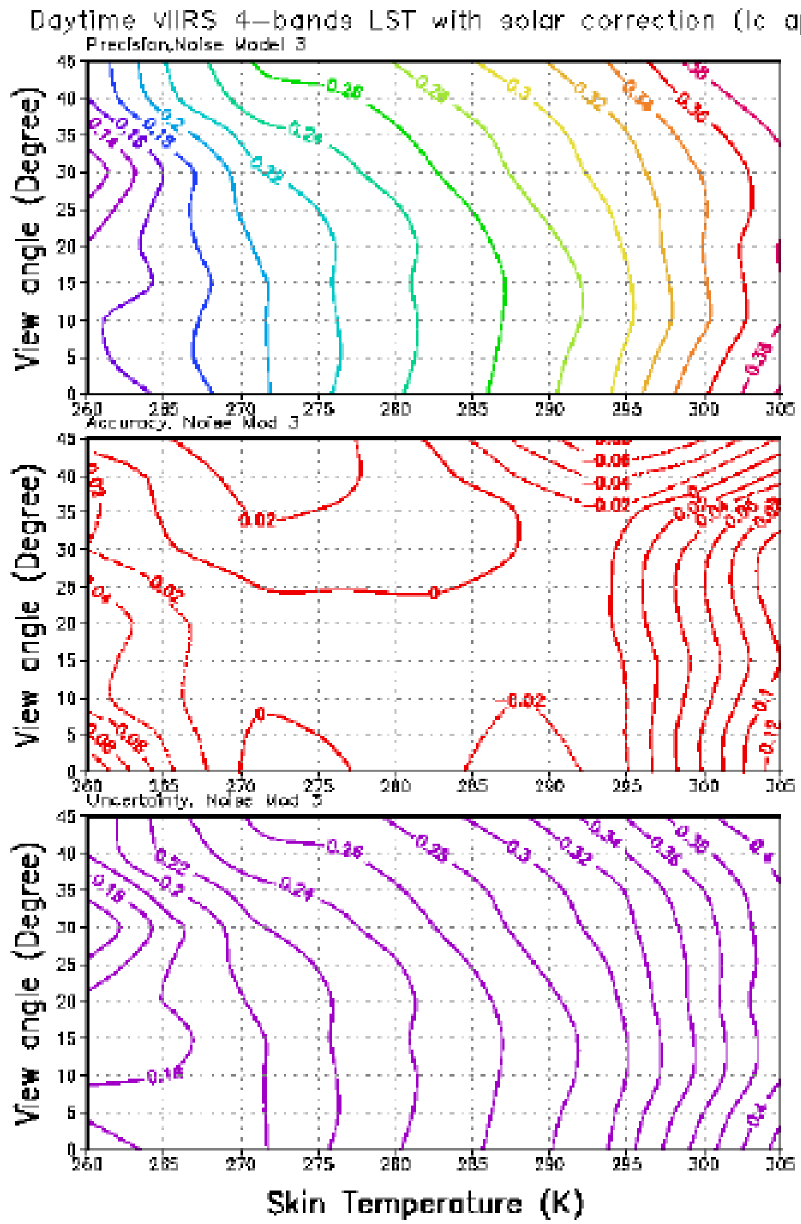

Figure 20. Daytime LST precision (upper panel), accuracy (middle) and uncertainty (bottom) distribution over satellite view angle and LST by using VIIRS-4 band algorithm (LC approach) with solar zenith correction.

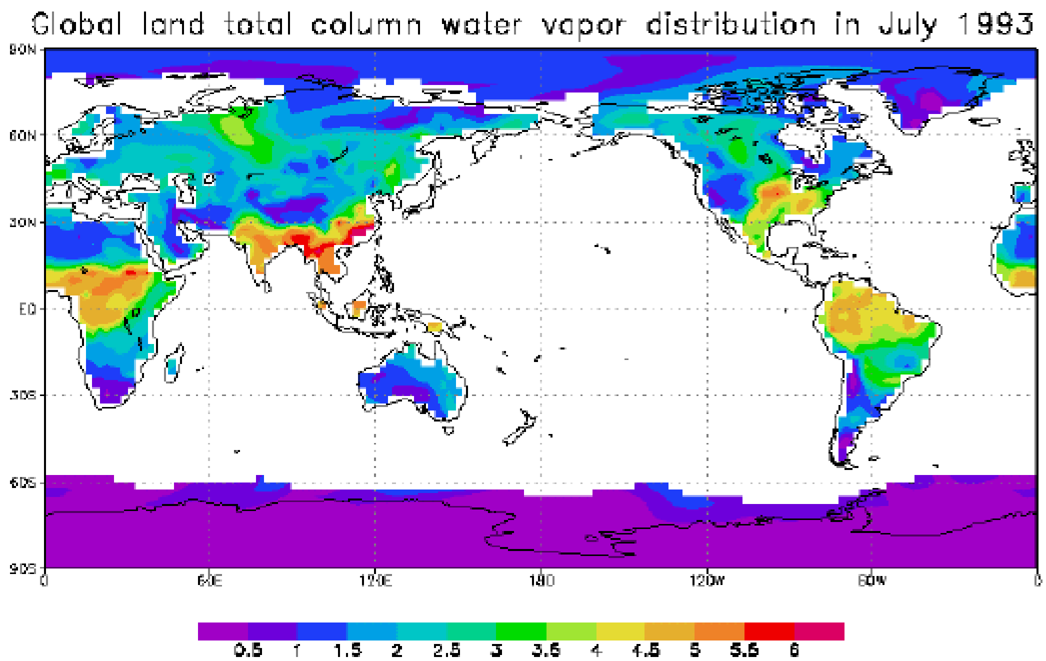

Figure 21. Total column water vapor distribution over land in our global dataset.

Water vapor's effect

In window channels, the main atmospheric effect comes from the water vapor absorption. So the total column water vapor amount has important effect to LST retrieval error. Figure 21 show the total column water vapor (TCWV) distribution in this global dataset.

Because more water vapor exists at higher temperature, as shown in figure 22, and LST bigger errors occurred at warmer temperature above 280 K. So we analyzed the relationship of LST retrieval error at temperature range 280-305 K with water vapor amount. Figure 23 shows the LST retrieval precision, accuracy and uncertainty distribution at warmer temperature (280-305 K) over total column water vapor and satellite view angle. In addition, split window algorithms with water vapor correction such as Becker and Li's (1995) and Coll and Caselles' (1997) were also tested. The 3-band algorithm with emissivity approach shows better precision than the generalized split window, the LST precision can meet the threshold 0.5 K at TCWV 1.0 to 5.5 g/cm^2, it can't meet the threshold at TCWV 0.5-1.0 g/cm^2 and greater than 5 g/cm^2. It increases with the TCWV amount and the view angle for TCWV greater than 4.5 g/cm^2.

One point that needs to be especially noted is that the LST precision is worse at TCWV 0.5-1.0 g/cm^2. These retrievals correspond to rock, sand, desert or sea ice area. Harris and Mason (1992) revealed that for a given change in surface temperature ΔT_0, resulting in changes in brightness temperatures in the two wavebands has the following relationship:

$$\frac{\Delta T_2}{\Delta T_1} = \frac{\varepsilon_2}{\varepsilon_1} \frac{\tau_2(0, p_0)}{\tau_1(0, p_0)}$$

$$\tau_\lambda(0,p_0) = exp(-k_{w\lambda}U_w(0,p_0))exp(-k_{o\lambda}U_o(0,p_0))$$

So surface emissivities as well as atmospheric transmittance changes cause brightness temperature change. If we divide the absorbing gases into water vapor and other gases

$$\frac{\Delta T_2}{\Delta T_1} = \frac{\varepsilon_2}{\varepsilon_1} exp((k_{w1} - k_{w2})U_w(0,p_0)\,exp((k_{o1} - k_{o2})U_o(0,p_0))$$

Where $k_{W\lambda}$ and KO_λ are the band–averaged absorption coefficients for water vapor and other gases, respectively; U_w $(0,p_0)$ and U_o $(0,p_0)$ are the total column contents of water vapor and other gases, respectively. Suppose the magnitude $(k_{w1}-k_{w2})$ Uw $(0,p_0)$ is small, and it is reasonable to take the first-order expansion, As U_w $(0,p_0)$ is the total column water or precipitable water W, so we have

$$\frac{\Delta T_2}{\Delta T_1} \approx \frac{\varepsilon_2}{\varepsilon_1}(1 + KW + const.)$$

So surface emissivity and atmospheric total column water vapor cause the brightness temperature change and therefore cause LST retrieval error. At TCWV 0.5-1.0 g/cm^2, the emissivity change at the 3.75 and 4.005 µm bands over rock, sand and desert cause LST retrieval error. This is also why LST precision by the 4-band LST algorithm with emissivity approach is greater than 0.5 K at the warmer temperature above 290 K.

Conversely the VIIRS-4 band algorithm by land cover approach shows LST precision can meet the threshold 0.5 K at all TCWV range and all view angles, shown as Figure 24. This is because this method overcomes the surface emissivity’s effect.

Figure 22. Water vapor vs. surface skin temperature distribution.

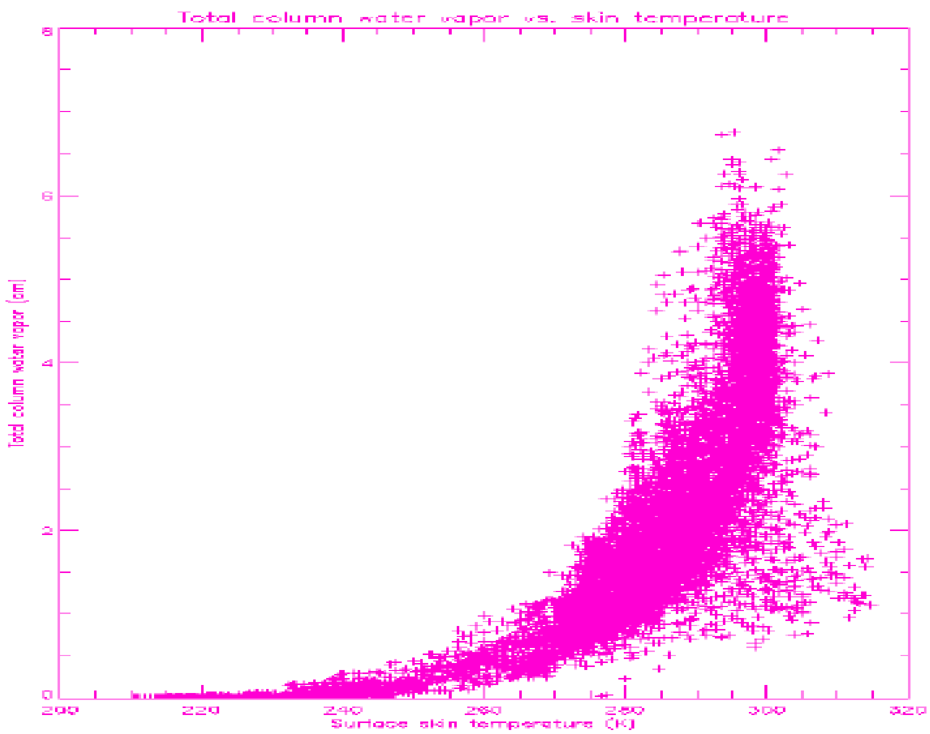

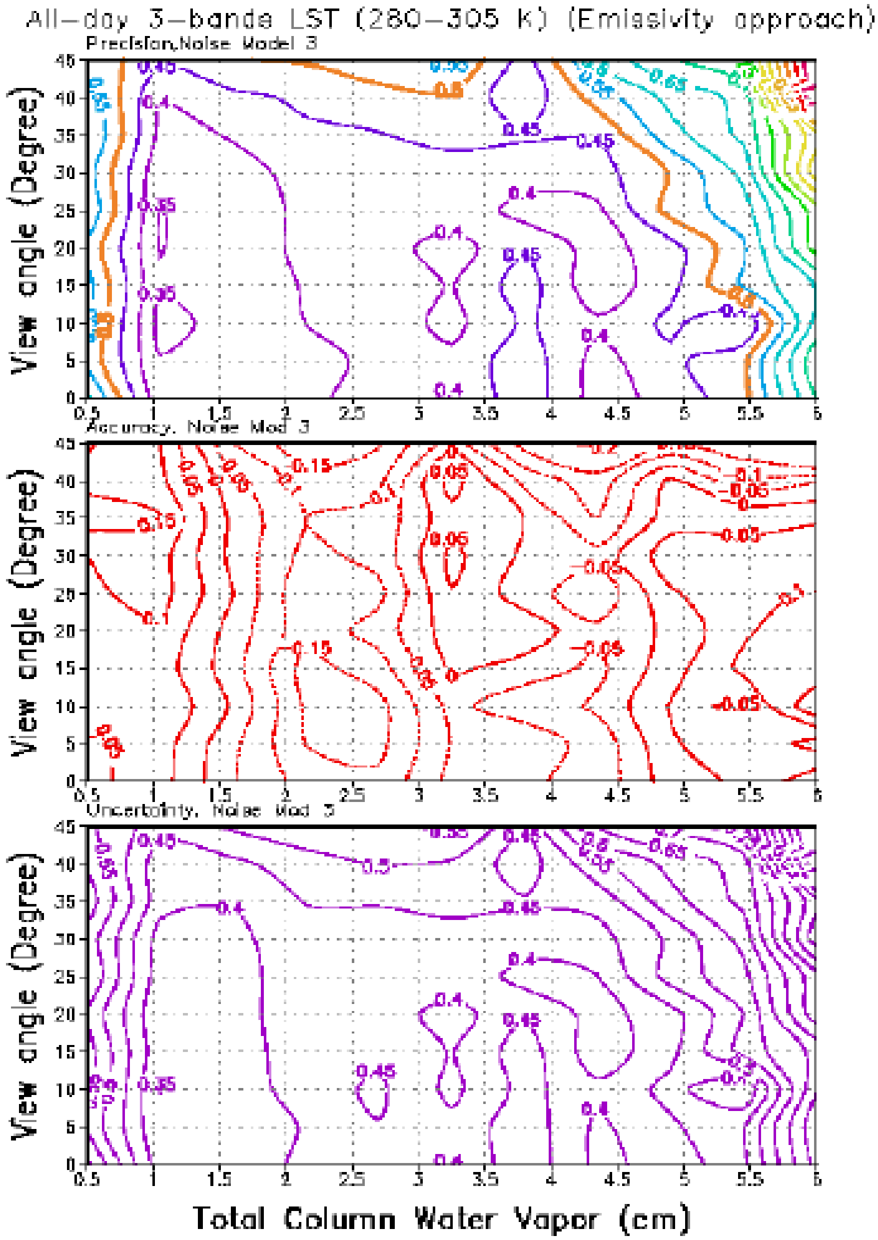

Figure 23. The LST precision, accuracy and uncertainty distribution with the TCWV and view angle by using the 3-band algorithm (emissivity approach).

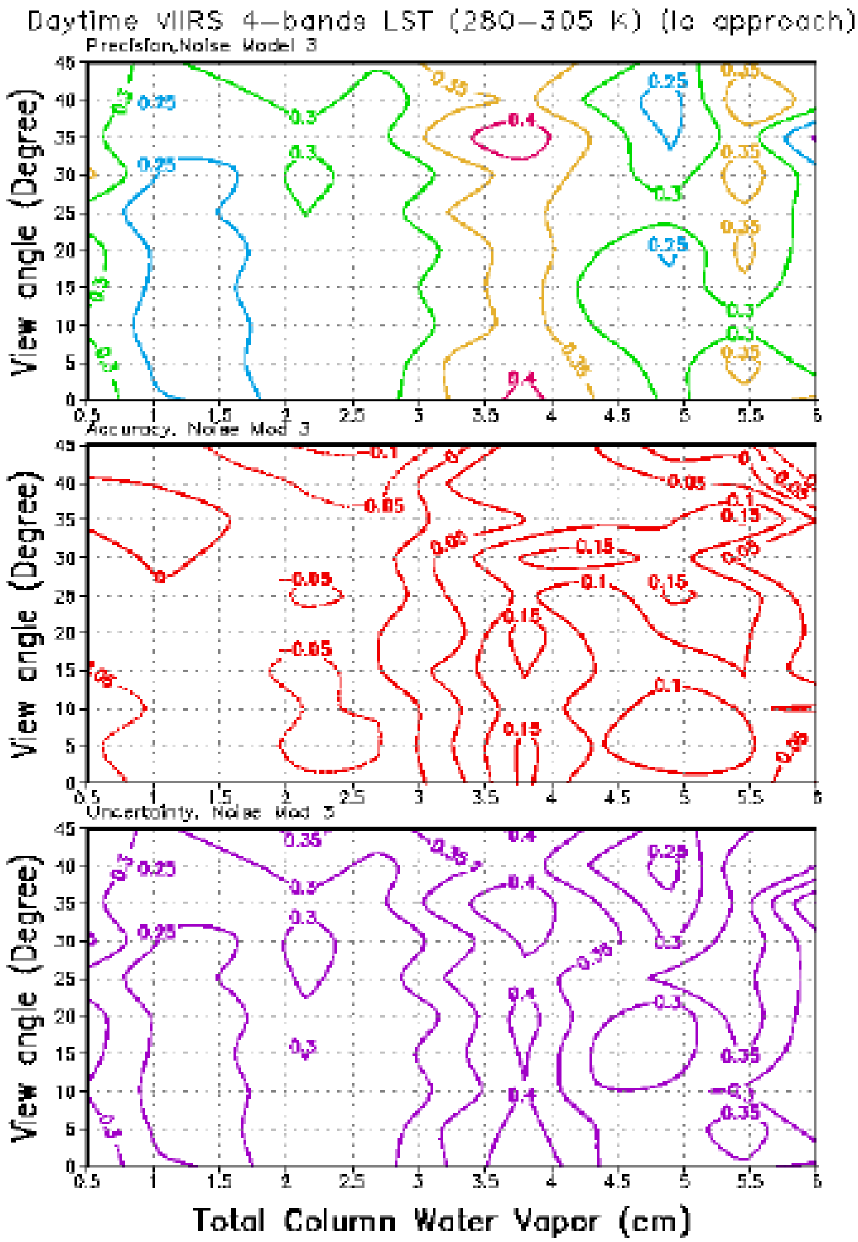

Figure 24. The LST precision, accuracy and uncertainty distribution with the TCWV and view angle by using the VIIRS 4-band algorithm (Land cover approach).

3.3.5 Validation problem

All of the tests above were performed based on simulation data, i.e., the truth LST was supposed to be known. For real-time data, the validation of global LST retrievals from satellite measurements is problematic since satellites measure skin temperature while ground truths provided by the global observational system are shelter temperatures. Although skin LSTs from a few field sites – such as the First International Satellite Land Surface Climatology Project (ISLSCP) Field Experiment (FIFE) – are now available (Prata, 1994; Wan and Snyder, 1996), they are not globally representative. Prata (1994) and many others have addressed the difficulty of obtaining ground truth LST. *In situ* LSTs can be measured with contact thermometers, as well as thermal infrared spectrometers. The contact thermometers measure an LST at a point, while the satellites measure the mean LST over a pixel area. The LST may vary significantly within a pixel area, and therefore, a single pixel may require the use of a number of thermometers.

In reality, both spatial and time variability of land surface temperatures is greater than that of sea surface temperature. This made the validation of LST retrieval from satellite data more difficult than with SST validation. Weng and Grody, (1998) tried to use shelter temperature in the early morning to validate LST retrieval from satellite SSM/I data. They found that the difference between surface skin temperature and shelter temperature is lowest at early morning. This validation, however, is limited to early morning. Another validation problem is the time. The number of *in situ* observations that match the satellite measurement in both time and space will be small: the *in situ* LST was not observed at the exact time when the satellite passed.

3.4 ALGORITHM SENSITIVITY STUDIES

3.4.1 Emissivity

Errors in emissivity have a strong effect on the LST retrieval by using those algorithms that depend on surface emissivity. Figure 25 shows the LST precision error vs. temperature distribution for generalized split window and new VIIRS-3 bands algorithm with 0.005-emissivity error.

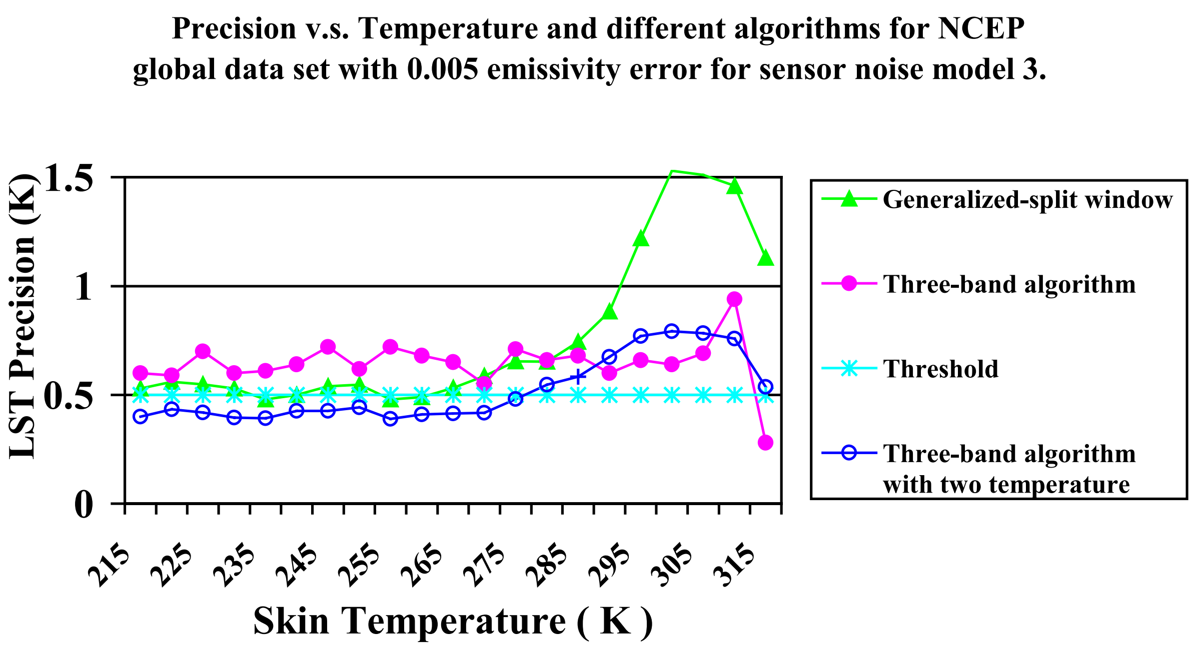

Figure 25. LST precisions vs. skin LST with 0.005 emissivity error.

As we can see from figure 25, for those algorithms which depend on surface emissivity, such as generalized split windoiw and new VIIRS- 3 bands algorithm, even with 0.005 emissivity error, the LST retrieval precision can't meet the threshold for almost all temperature range, especially for warmer temperature. For these reasons we have adopted a Land Cover approach.

3.4.2 Land Cover

Our baseline algorithm VIIRS-4 band algorithm depends on an accurate knowledge of land surface types. The VIIRS vegetation index EDR accuracy requirement is 70%. But, usually, above 80% accuracy can be achieved by using neural networks or decision tree algorithms. When we did an experiment with a 20% land cover classification error, the LST retrieval process is a little bit worse, but it can still meet the threshold of 0.5 K. This is because land cover classifications by using neural networks or decision trees misclassify to a similar surface type that still has similar emissivity characteristics. For instance, broadleaf forests may be misclassifying as pine forests, pine brush as broadleaf brush, or wet soil as scrub soil. Grass, however, cannot be classified as rock or sand. So this is why an algorithm based on surface types may not cause great errors, even with a 20% land cover classification error, see figure 26.

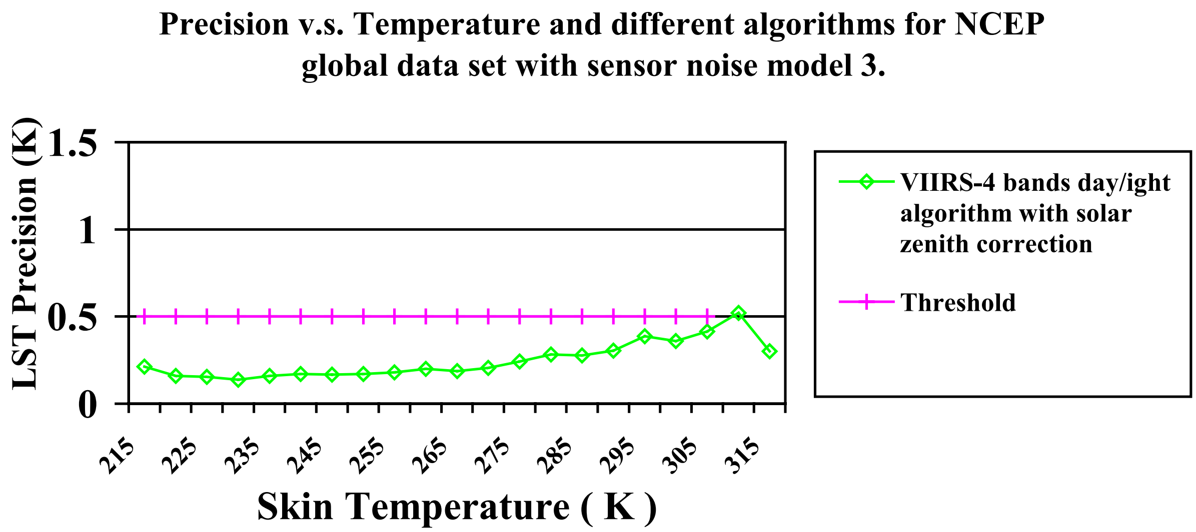

Figure 26. LST precision vs. temperature by using VIIRS –4 bands day/night algorithm with 20% land cover classfication error.

3.5 PRACTICAL CONSIDERATIONS

3.5.1 Numerical Computation Consideration

In order to stay current, an average processing of 10,000 pixels per second must be performed. A database from accurate radiative transfer simulations needs to be established, and a look-up table and interpolation scheme should be developed to speed the process. The physical retrieval must run a radiative transfer model. Current computers may only process a few pixels per second. Therefore, the implementation of the physical retrieval will depend on the speed of the computers used.

3.5.2 Programming and Procedural Considerations

Look-up tables will be used to increase the computational efficiency. Registration and re-sampling into horizontal cell size will be made after the level-2 LST processing. Parallel processing is allowed for the LST retrieval.

3.5.3 Quality Assessment and Diagnostics

A number of parameters and indicators will be reported in the LST product as retrieval diagnostics. LST maps and statistical information will be reviewed for quality assessment. Quality flags that indicate the confidence in LST processing will be provided. They will be determined by comparing LST values from different algorithms (e.g., regression and physical retrievals, or different regression methods).

3.5.4 Exception Handling

Cloud pixels identified by the cloud mask will be skipped. Pixels with bad data will also be skipped and flagged.

3.6 ALGORITHM VALIDATION

3.6.1 Pre-Launch Validation

The atmospheric correction algorithm will be derived pre-launch by radiative transfer modeling to simulate the VIIRS infrared channel measurements. Selected radiosondes from the operational network stations or field campaigns will be used in VIIRS simulations for the development of the atmospheric correction algorithm. Measurements from the portable radiometers and a TIR spectrometer will be used to characterize the surface temperature fields and validate the atmospheric correction algorithms. The assimilated meteorological fields provided by NCEP and ECMWF provide a valuable description of surface temperature over land. These fields will be used in conjunction with radiative transfer modeling to simulate the VIIRS measurements, validate the radiosonde data, and provide direct input to the radiative transfer modeling process.

Measurements from AVHRR, the Along Track Scanning Radiometer (ATSR), and MODIS will be used in the pre-launch phase to study the error characteristics of the LST retrieval.

3.6.2 Post-Launch Validation

The post-launch validation activities are designed primarily to test the LST retrieval algorithm. Several fundamentally different data sets are needed to provide an adequate sampling of the atmospheric conditions and LST to validate the VIIRS IR radiance and retrieved LST fields. Highly focused field experiments are necessary to understand the atmospheric processes that limit the accuracy of the retrieved LST. Sites will be selected globally to validate VIIRS LST retrieval. (MODIS LST ATBD, version 3.2). Relatively flat areas of highly unmixed surface type will yield the highest quality measurements for validation. Portable radiometers and a TIR spectrometer will be calibrated with the same blackbody radiation source. Long-term global data sets are necessary to provide a monitoring capability that would reveal calibration drift and the consequences of extreme atmospheric events. Validation is required over the lifetime of the NPOESS mission.

4.0 ASSUMPTIONS AND LIMITATIONS

A major limitation of the VIIRS LST retrieval is that it can only be done under clear sky conditions. The algorithm is based on this basic assumption.

5.0 REFERENCES

Becker, F. (1987): The impact of spectral emissivity on the measurement of land surface temperature from a satellite. *Int. J. Remote Sens*. 11: 369-394.

Becker, F., and Z. L. Li (1990). Toward a local split window method over land surface. *Int. J. Remote Sens*. 11, 369-393.

Becker, F., and Li, Z. -L. (1995) Surface temperature and emissivity at various scales: definition, measurement and related problems. *Remote Sens. Rev.* 12:225-253.

Berk, A., L. S. Bemstein, and D. C. Robertson (1987). MODTRAN: A moderate resolution model for LOWTRAN. Rep. GLTR-89-0122, Burlington, MA: Spectral Sciences, Inc.

Camillo, P. J., 1991: "Using one- or two-layer models for evaporation estimation with renotely sensed data" in Land Surface Evaporation: Measuremnts and Parameterization, ed. T. J. Schmugge and J. C/ Andre, New York: Springer-Verlag.

Caselles, V., E. Valor, C. Coll, and E. Rubio (1997). Thermal band selection for the PRISM instrument 1. Analysis of emissivity-temperature separation algorithms. *J. Geophys. Res*., 102, 11145-11164.

Coll, C., and Caselles, V. (1997), A split-window algorithm for land surfaces temperature from Advanced Very High-Resolution Radiometer data: Validation and algorithm comparison. *J. Geophys. Res*. 102: 16,697-16,713.

Coll, C., Caselles, V., Sobrino, J.A., and Valor, E. (1994), On the atmospheric dependence of the split-window equation for land surface temperature. *Int. J. remote Sens*. 15 (1): 105-122.

Cornette, W. M., P. K. Acharya, D. C. Robertson, and G. P. Anderson (1994). Moderate spectral atmospheric radiance and transmittance code (MOSART). Rep. R-057-94(11-30), La Jolla, CA: Photon Research Associates, Inc.

Crag, R., M. Sugita, and W. Brutsaert, 1995: Satellite-derived surface temperature with boundary layer temperatures and geostrophic winds to estimate surface energy fluxes, J. Geophys. Rev., vol. 100, no. D12, 25447-25451.

Diak, G. R. and M. S. Whipple, 1993: Improvements to models and methods for evaluating the land-surface energy balance and effective roughness using radiosonde reports and satellite-measured skin temperature data, Agricul. and Forest Meteorol., vol. 63, no. 3-4, 189-218.

Dozier, J., and Z. Wan (1994). Development of practical multiband algorithm for estimating land surface temperature from EOS/MODIS data. *Adv. Space Res*., 13, 81-90.

Harris, A.R., and I.M. Mason (1992). An extension to the split-window technique giving improved atmospheric correction and total water vapor. Vol. 13, no. 5, 881-892.

Jackson, R. D., R. J. Reginato, and S. B. Idso, 1977: Wheat Canopy temperature: a practical tool for evaluating water reqirements, *Water Resour. Res*., vol. 13, 651-656.

Kimura, F. and A. P. Shimiru, 1994: Estimation of sensible and latent heat fluxes from soil surface temperature using a linear air land heat transfer model, *J. Appl. Meteorol.* , vol. 33, no. 4, 477-489.

Kealy, P. S., and S. J. Hook (1993). Separating temperature and emissivity in thermal infrared multispectral scanner data: Implications for recovering land surface temperature. *IEEE Trans. Geosci. Remote Sens*., 31, 1155-1164.

Kneizys, F. X., E. P. Shettle, L. W. Abreu, J. H. Chetwynd, G. P. Anderson, W. O. Gallery, J. E. A. Selby, and S. A. Clough (1988). Users guide to LOWTRAN7. Rep. AFGL-TR-88-0177, Bedford, MA: Air Force Geophys. Lab.

Konzemann, T., 1994. Radiation conditions on the Greenland ice sheet. Zurcher Geographische Schriften. Geographical Institute ETH 56, 124.

Li, Z. L., and F. Becker (1993). Feasibility of land surface temperature and emissivity determination from AVHRR data. *Remote Sens. Environ*, 43, 67-85.

Mannstein, H. (1987). Surface energy budget, surface temperature and thermal inertia in Remote Sensing Applications. In Meteorology and Climatology, ed. R.A. Vaughan and D. Reidel. I, NATO ASI Ser. C: Math. Phys. Sci. Vol 201, pp. 391-410, Dordrecht Netherlands: A Reidel Publishing Co.

Meehl, G. A., Influence of the land surface in the Asian summer monsoon: extenal conditions versus internal feedbacks, J. Climate, vol. 7, 1033-1049.

Prata, A. J. (1993). Land surface temperature derived from the Advanced Very High Resolution Radiometer and the Along-Track Scanning Radiometer I. Theory. *J. Geophys. Res*., 98, 16689-16702.

Price, J. C. (1984), Land surface temperature measurements form the split window channels of the NOAA-7/AVHRR. J. Geophys. Res. 89: 7231-7237.

Running, S. W., 1991: Computer simulation of regional evapotranspiration by integrating landscape biophysical attributes with satellite data, in Land Surface Evaporation: Measurements and Parameterization, ed. T. J. Schmugge and J. C. Andre, New York: Springer-Verlag.

Running, S. W., C. Justice, V. Salomonson, D. Hall, J. Barker, Y. Kaufman, A. Strahler, A. Huete, J.-P. Muller, V. Vanderbilt, Z. Wan, and P. Teillet, 1994: Terrestrial remote sensing science and algorithms planned for EOS/MODIS, Int. J. Remote Sens., vol. 15, no. 17, 3587-3620.

Sellers, P.J., F.G. Hall, G. Asrar, D.E. Strebel, and R.E. Murphy (1998). The first ISLSEP Field, Experiment (FIFE). Bull. *Amer. Meteorol. Soc.,* Vol. 69, no. 1, 22-27, 1988.

Schmugge, T. J. and F. Becker, 1991: " Remote sensing observations for the monitoring of land surface fluxes and water budgets," in Land Surface Evaporation: Measurments and Parameterization, ed. T. J. Schmugge and J. C. Andre, New York: Springer-Verlag.

Vidal, R. C. and B. L. Blad, 1991: Atmospheric and emissivity correction of land surfcae temperature measured from satellite using gorund measurments or satellite data, Int. J. Remote Sens., vol. 12, no. 12, 2449-2460.

Vining, R. C. and B. L. Blad, 1992: Estimation of sensible heat flux from remotely sensed canopy temperatures, *J. Geophys. Res*., vol. 97, no. D17, 18951-18954.

Wan, Z., and J. Dozier (1996). A generalized split-window algorithm for retrieving land-surface temperature from space. *IEEE Trans. Geosci. Remote Sens*., 34, 892-905.

Wan, Z., and W. Snyder (1996). MODIS Land-Surface temperature algorithm theoretical basis document. MODIS ATBD

Watson, K. (1992). Two temperature method for measuring emissivity. *Remote Sens. Environ*, 42, 117-121.

Weng, F., and N. Grody (1998), Physical Retrieval of land surface temperature using the special sensor microwave imager. *J. Geophys. Res*., 103: 8839-8848.

Yu, Y. D. , A. Rothrock, and R. W. Lindsay, 1995: Accuracy of sea ice temperature derived from the advanced very high resolution radiometer, *J. Geophys. Res*., vol. 100, no. C3, 4525-4532.

Zhang, L., Lemeur, and J. P. Goutorbe, 1995: A one-layer resistance model for estimating regional evapotranpiration using remote sensing data, in Agricul. and Forest Meteorol., vol. 77, 241-261.